>200 Gbit/s Multicore fiber-based short-reach networks employing Kramers-Kronig receivers

João Miguel Caetano André

Master in Telecommunications and Computer Engineering

Supervisor
PhD Tiago Manuel Ferreira Alves, Assistant Professor
Iscte - Instituto Universitário de Lisboa

Co-Supervisor
PhD Adolfo da Visitação Tregeira Cartaxo, Full Professor
Iscte - Instituto Universitário de Lisboa

November, 2021

iscte

**TECNOLOGIAS
E ARQUITETURA**

>200 Gbit/s Multicore fiber-based short-reach networks employing Kramers-Kronig receivers

João Miguel Caetano André

Master in Telecommunications and Computer Engineering

Supervisor
PhD Tiago Manuel Ferreira Alves, Assistant Professor
Iscte - Instituto Universitário de Lisboa

Co-Supervisor
PhD Adolfo da Visitação Tregeira Cartaxo, Full Professor
Iscte - Instituto Universitário de Lisboa

November, 2021

For my parents

Acknowledgment

Resumo

Este trabalho propõe uma rede de curto alcance com um débito binário por utilizador superior a 200 Gbit/s utilizando fibras multi-núcleo (MCF) e recetores de Kramers-Kronig (KK) como solução alternativa às redes de curto alcance de elevada capacidade, usadas em data centers (DC). Os recetores KK combinam modulações de ordem elevada, usadas em recetores coerentes, com a rentabilidade da deteção-direta. O uso de MCF tem sido proposto para aumentar a capacidade e a densidade de conectores em DCs. Combinando o uso de ambas as tecnologias, é possível aumentar a capacidade de redes de curto alcance a um baixo custo obtendo um elevado desempenho.

Neste trabalho, é feita uma comparação entre diferentes versões de recetores KK na presença de diafonia entre núcleos. É considerado um recetor KK ideal e duas variações, uma onde a corrente foto-detetada é desacoplada e uma outra onde a corrente é limitada a um mínimo com a intenção de aumentar o desempenho do recetor. A probabilidade de indisponibilidade é usada como métrica para avaliar o desempenho do sistema e é estimada através de simulação de Monte Carlo e error vector magnitude (EVM). Os resultados mostram que é possível utilizar a EVM para estimar a probabilidade de indisponibilidade com um erro inferior a 0.8 dB para uma probabilidade de 10^{-3}. Ainda, o desempenho do recetor KK ideal é inferior aos restantes, pois este não atenua o número de vezes que o sinal se aproxima da origem, ao contrário dos outros recetores.

Palavras-chave: Fibras multi-núcleo; recetores Kramers-Kronig; redes de curto alcance; probabilidade de indisponibilidade

Abstract

This work proposes a short-reach network with more than 200 Gbit/s bit-rate per user using weakly-coupled multicore fibers (MCF) and Kramers-Kronig (KK) receivers with the goal of providing an alternative solution for high capacity short-reach networks, usually found in data centers (DC). The use of KK receivers combines the high order modulation formats, commonly found in coherent detection receivers, with the cost-effectiveness of direct-detection (DD), two important features in short-reach networks. The use of MCF has been proposed to increase the capacity and density of optical interconnects in DCs. The combined use of these two technologies significantly increases the capacity of short-reach networks while being cost effective and highly performing.

A comparison of the performance of three different KK receiver implementations in the presence of inter-core crosstalk (ICXT) is carried out. The different KK receivers are the ideal KK receiver and two variations, one where the photo-current is AC coupled and another where the photo-current is clipped to increase the receiver performance. The outage probability is used as a metric for the performance of the system, it is estimated by Monte Carlo simulation and by the error vector magnitude (EVM). The results show that it is possible to estimate the outage probability of the system using the EVM with an estimation error not exceeding 0.8 dB for an outage probability of 10^{-3}. In addition, the ideal KK receiver has the worst performance since it fails to mitigate the negative excursion of the signal close to zero.

Keywords: Multicore fibers; Kramers-Kronig receivers; short-reach networks; outage probability

Contents

List of Figures

List of Tables

List of Acronyms

APD	Avalanche photo-diode
AWG	Additive white Gaussian
BER	Bit error rate
CD	Chromatic dispersion
CSPR	Carrier-to-signal power ratio
CW	Continuous wave
DC	Data Center
DCF	Dispersion-compensating fiber
DD	Direct-detection
DSP	Digital signal processing
EDFA	Erbium-doped fiber amplifier
EVM	Error vector magnitude
FEC	Forward error correction
GVD	Group velocity delay
ICXT	Inter-core crosstalk
KK	Kramers-Kronig
LPF	Low pass filter
MCF	Multicore fiber
MIMO	Multiple-input multiple-output
MMF	Multi-mode fiber
MZM	Mach-Zhender modulator
NZDSF	Nonzero dispersion shifted fiber

PAM	Pulse amplitude modulation
PAPR	Peak-to-average power ratio
PDM	Polarization division multiplexing
PMD	Polarization mode dispersion
PSD	Power spectral density
QAM	Quadrature amplitude modulation
RC	Raised cosine
RMS	Root-mean-square
RPS	Random phase shift
RRC	Root-raised cosine
SDM	Space division multiplexing
SE	Spectral efficiency
SMF	Single-mode fiber
SNR	Signal-noise ratio
SSB	Single-side band
SSBN	Signal-to-signal beat noise
STAXT	Short-term average crosstalk
WC-MCF	Weakly-coupled multicore fiber
WDM	Wavelength-division multiplexing
XT	Crosstalk

List of Symbols

A	Continuous wave component amplitude
$a(t)$	Optical signal
$\overline{\beta}_n$	Average of the intrinsic propagation constants of the two polarization directions
β_r	Roll-off factor
$\Delta\overline{\beta}_{0,mn}$	Difference of propagation constants at $\omega = 0$
B	System's bandwidth
B_{GB}	Guard band between the optical carrier and the information bearing signal
B_{RRC}	RRC signal bandwidth
$B_{e,n}$	Equivalent noise bandwidth
C	Channel Capacity
c	Speed of light in a vacuum
ΔD_{mn}	Difference of dispersion parameters between cores
d_{mn}	Average walkoff parameter
$E_{LO}(t)$	Optical field of the local laser
$E_{SSB}(t)$	Optical field of the SSB signal
$E_s(t)$	Optical field of the information bearing signal
$\vec{E}_{ICXT}(t)$	Optical ICXT field at the output of the test core
$\vec{E}_m(t)$	Optical signal launched to the interfering core
$\vec{E}_n(t)$	Optical signal launched to the test core
$\vec{E}'(t)$	Optical field at the output of the test core
$e_{in}(t)$	Input of the IQ modulator

$e_{lin,comp}(t)$	Output of the linearised MZM
$e_{out}(t)$	Output of the IQ modulator
$e_{out,comp}(t)$	Output of the MZM
$\text{erfc}(x)$	Complementary error function of x
$F_{b,pol}(\omega)$	Transfer function that models the ICXT from the input of the interfering core to the output of the test core
f_s	Simulation bandwidth
$\mathcal{H}\{u(t)\}$	Hilbert transform of $u(t)$
$H_R(f)$	Receiver filter transfer function
$h_{RRC}(t)$	RRC filter impulse response
$i(t)$	Photo-current at the output of the p-i-n
$i_I(t)$	Current of the phase component of the signal
$i_Q(t)$	Current of the quadrature component of the signal
$\overline{K}_{nm}$	Core coupling coefficient
λ	Optical wavelength carrier
L	Fiber length
$\log(x)$	Natural logarithm of x
M	Modulation order of the QAM signal
M_s	Number of different spacial paths
$\max(x)$	Maximum value of x
N	Number of RPS
N_c	Number of interfering cores
N_s	Number of symbols in the sequence
$N_{samples}$	Number of samples per symbol
NEP	Noise equivalent power
$n(t)$	Electrical noise
$\phi_{b,pol}^{(k)}$	Phase of the k-th RPS

P_c	Optical power of the signal launched to the fiber core
P_m	Power of the interfering core
P_n	Power of the test core
P_{out}	Outage probability
R_λ	P-i-n responsivity
R_s	Symbol rate
σ_c^2	Electrical noise variance
$S_c(f)$	RC filter transfer function
S_{mn}	Skew between cores
$STAXT_n(t)$	STAXT in the n-th time fraction
$s(t)$	Output of the KK algorithm
$s_0[k]$	Normalized amplitude of the k-th received symbol
$s_i[k]$	Normalized amplitude of the k-th symbol of the ideal constellation
T_s	Symbol period
$\#TF_{out}$	Number of time fractions with higher BER than the threshold
$\#TF_{total}$	Number of elapsed time fractions
$V_{bias,MZM}$	Bias point of the MZM
V_{sv}	Switching voltage of the MZM
$v_{comp}(t)$	Driving signal of the MZM
X_c	ICXT level
$\overline{x}$	Average of x
z_k	Position of the k-th RPS

CHAPTER 1

Introduction

With the ever-growing demand for internet connectivity and with projections for at least double the speed of fixed broadband and triple the speed of mobile network connections by 2023 [1]. With the projected growth of 30% compound annual growth rate in machine-to-machine communication from 2018 to 2023 [1] and the introduction of 5G technology on the market with 13.1 billion devices in 2023 [1], the demand for bigger and more capable data centers (DC) will increase. However, a capacity crunch in fiber, the resources of the underlying network becoming insufficient [2], will inevitably compromise the growth requiring new and improved solutions to satisfy the demand.

This work proposes a new short-reach optical network using space division multiplexing (SDM) and Kramers-Kronig (KK) receivers in order to increase the capacity per user beyond 200 Gbit/s.

Within this work the main issues of this type of network using these receivers are addressed. Further, the inter-core crosstalk (ICXT) generated by the multicore fiber (MCF) has an impact on the performance of the system which has not yet been studied.

Some original contributions are presented in this work, mainly the study of the impact of the ICXT on the performance of three variations of the KK algorithm and the analysis of the performance of the proposed network. The variations of the KK algorithm are the ideal variant, the AC coupled KK algorithm, and the clipping enhanced KK algorithm, with each one having different advantages/disadvantages.

1.1. Objectives

The main objective of this work is to unlock the necessary capacity for next generation optical access networks. To accomplish this, a short-reach network with over 200 Gbit/s per user employing SDM and KK receivers is proposed. The following objectives are pursued:

- Integrate the software platform for simulation of a short-reach, over 200 Gbit/s, SDM optical fiber network employing KK techniques for receiver linearization.
- Identify the main operational issues of the proposed short-reach SDM network.
- Assess the impact of the random nature of the ICXT over time on the performance of the proposed short-reach network employing KK receivers.

To accomplish the aforementioned objectives, the following tasks are executed:

- Development of a Matlab software that generates and detects a 200 Gbit/s optical signal.
- Identification of the ideal and practical implementation of the KK receiver.
- Inclusion of multicore fiber propagation in the Matlab software.
- Development of a digital signal processing equalizer for dispersion compensation.
- Development of simulations in order to specify reach and capacity requirements achievable for the proposed short-reach network.

1.2. Structure of this work

This work is divided in four chapters where the different research questions are answered.

Chapter 2 comprises a review of the main body of literature about technologies employed in this work. It presents the main requirements and challenges of the networks employed in DCs, why SDM technology was proposed to solve the future capacity crunch of optical fiber network, the different types of SDM available today and an in-depth review of the different KK algorithms along with their advantages and disadvantages.

Chapter 3 presents the system model of the proposed short-reach network with a comprehensive description of all the system's blocks, the differences in the system when using the different KK algorithms, how the Matlab simulator was developed and the verification that all the system blocks were correctly implemented.

Chapter 4 presents the impact of the ICXT on the system for all the different variations of the KK receiver and the outage probability for the considered variations.

Chapter 5 presents the major conclusions from the analysis presented in this work and suggests some future work.

CHAPTER 2

State of the art

This chapter presents a review of several technologies used in optical communications. In section 2.1 current problems and some DC specifications are introduced. Section 2.2 presents a review of the fiber technology through the decades with special emphasis on new proposed ways of increasing fiber capacity, namely space division multiplexing in section 2.3. Lastly, an analysis of several optical receivers is presented in section 2.4 where advantages and drawbacks of several different types of receivers are scrutinized, particularly Kramers-Kronig receivers.

2.1. Data center

In recent years people have changed how they use the internet. The growth of Content Distribution Networks like Netflix, the birth of software as a service and cloud services fundamentally changed how DCs work. To accommodate the change to hyper-scale DCs the architecture shifted to a flatter, more scalable architecture [3].
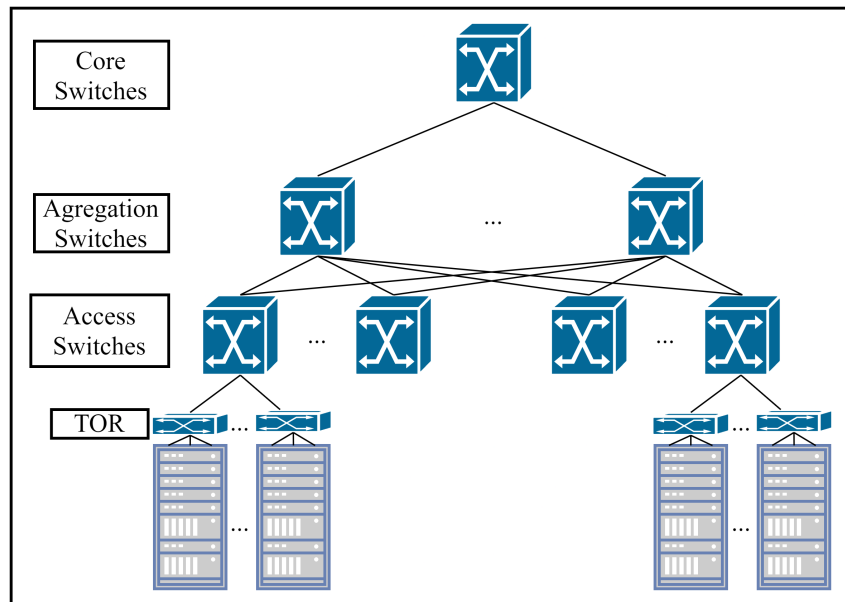
FIGURE 2.1. Three tiers data center architecture.

DCs went from a 3 tier structure that favors north-south traffic, from outside the DC to the server, to a 2 tier structure that facilitates east-west traffic, server to server, or DC to DC. As seen in fig. 2.1, DCs had a tree-shaped topology with redundant core and
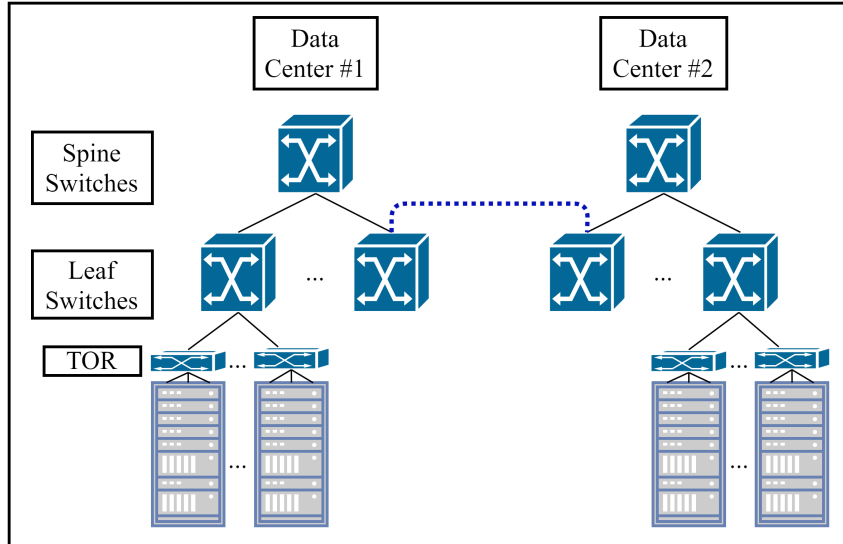
FIGURE 2.2. Two tiers data center architecture.

aggregation switches. Core switches connected one DC to another and traffic from server to server had to travel up to the core switches. This process is extremely inefficient for east-west traffic and poses a scalability problem [4]. To solve this problem, DCs switched to a flat architecture shown in fig. 2.2. In this new architecture, two different DCs can be connected through multiple leaf switches to accommodate large amounts of traffic and are highly scalable because it is relatively easier to add more server racks and connect them to leaf switches than to add a rack to a tree-like structure [4, 3]. In this new architecture, it is possible to differentiate 2 types of links with different design requirements:

- Intra DC links: reach ≤10 km, operating near 1310 nm to minimizing chromatic dispersion with low power consumption, high-density interconnects, high bit-rate, and high-bandwidth being the main requirements [4]. However, these links cannot be amplified due to the aforementioned power consumption requirements [4]. Furthermore, this links currently employ coarse or LAN wavelength-division multiplexing (WDM).
- Inter DC links: reach ≤100 km, operating at 1550 nm using dense WDM with low power consumption, high bit rate, and with amplification allowed [4].

Nowadays DCs use optical transceivers based on IEEE 802.3 standard [5]. They use DD with either non-return to zero or 4-level pulse-amplitude modulation (PAM) pulses and are divided into 3 categories based on their speed [5]:

- 40G: using four lanes of 10 Gb/s NRZ signal with single-mode fiber (SMF) or multi-mode fiber (MMF) transmission fibers. If using SMF, coarse WDM is employed and a maximum reach of 10 km is possible, with two fibers employed, one for each direction, making one full-duplex system. If using MMF, four fibers in each direction are needed, and depending on the type of fiber, a maximum reach of 150 m is possible.

4

- 100G: Several configurations are available using different quantity and lane speeds with the possibility of employing forward error correction (FEC). Using MMF, a maximum reach of 100 m is possible. While employing SMF, a maximum reach of 10 km is achievable.
- 400G: there are 4 generations of 400G transceivers that use different amounts of lanes at different speeds. A maximum reach of 10 km over SMF is possible and 100 m over MMF.

However, DC interconnects are still a technology in development with new techniques being proposed such as using higher level PAM pulses [6, 7] or using coherent receivers with comparable energy consumption of that of a PAM-4 system [8].

2.2. Fiber technology
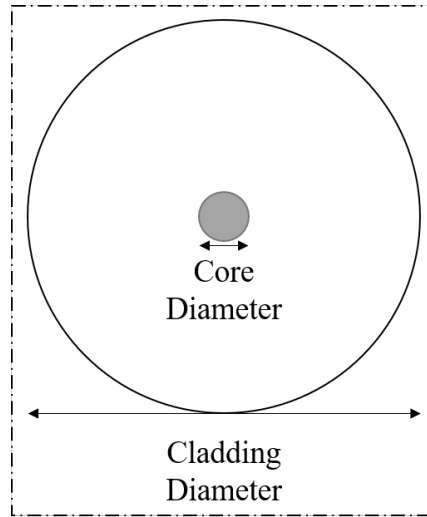
FIGURE 2.3. Single-core fiber cross-section.

In 1977, the first fiber optics field trial was conducted [9]. Since then, several types of fibers were created to leverage some transmission characteristics. However, one of the most deployed fiber types is standard single-mode fiber, described in [10] and, in fig. 2.3 a fiber cross-section is presented. The fiber is a waveguide composed of a core and cladding usually manufactured in silica with the material used in the core being doped, resulting in a higher refractive index [11]. Furthermore, fiber communications are impaired mainly by two effects, fiber loss and chromatic dispersion (CD).

The fiber loss is self-explanatory, power at the link end is less than the power at the beginning of the link. Material absorption and Rayleigh scattering contribute to the majority of losses present in silica fiber [11]. Furthermore, material absorption can be differentiated in intrinsic, caused by resonant vibration in silica molecules, and extrinsic, due to impurities in the material [11]. Rayleigh scattering is characterized by localized fluctuations in the fiber's refractive index causing optical power to be reflected [11].

CD is one effect responsible for pulse broadening and depends on fiber parameters such as refractive index difference and core radius. There are two main reasons for CD, one is that the refractive index of silica is frequency-dependent, which in turn causes the pulse to broaden as its frequency components are traveling at different speeds, and the other is called waveguide dispersion and consists of the different power distribution through the fiber diameter, core/cladding, causing the effective refractive index to change [11]. Hence, the construction of fiber with different chromatic dispersion parameter is possible and this allows CD to be controlled, commonly called dispersion management [11].

Dispersion management can be employed in different ways with the goal of controlling CD. In a precompensation scheme, the characteristics of the transmitted pulse are modified before the signal is launched into the fiber such that the degradation induced by CD is reduced or completely eliminated [11]. Dispersion management can also use two different types of fiber to control accumulated dispersion in the system [11]. A popular choice for submarine cables was nonzero dispersion shifted fiber (NZDSF) [12], defined in [13], which came with two different chromatic dispersion parameters: one slightly positive and another slightly negative. This meant that two transmission fibers could be used, keeping the accumulated dispersion to a minimum. On land, with the creation of slope matched dispersion-compensating fiber (DCF) [14, 15], with higher negative chromatic dispersion than NZDSF, DCF could be deployed in spools in conjunction with erbium-doped fiber amplifiers (EDFA) [12]. In recent times, with the advent of coherent transmission, CD is compensated in the receiver using DSP algorithm, making this a postcompensating scheme. Coherent systems accumulate CD instead of managing it, keeping the nonlinear effects low and simplifying the deployment [12].

Another effect present in silica fibers is polarization mode dispersion (PMD). This effect also causes pulse broadening due to fiber birefringence. In the fabrication process, the fiber does not have a perfectly cylindrical shape, which causes the orthogonal polarization of the fundamental propagation mode to disperse [11]. With the advance of the manufacturing process [16], lower PMD values were available, hence, only in long-range systems PMD has a noticeable effect. However, with the demand for higher bit-rate per wavelength and far reach systems, WDM was introduced, which, in turn, led to higher power levels and more channels present in the fiber. This meant that nonlinear effects started being relevant. Some nonlinear effects are:

- Stimulated light scattering: Brillouin and Raman scattering are both present in silica fibers and the scattering process results in a photon of lower energy. This photon results in loss of power in the incident frequency [11].
- Nonlinear phase modulation: Self-phase modulation and cross-phase modulation occur because the fiber refractive index is intensity field-dependent [11].
- Four-wave mixing: Due to the power dependence of the refractive index, three optical fields can generate several others if they co-propagate in close to zero dispersion. This process results in power transfer to other channels in the system,

commonly known as crosstalk, degrading the signal previously present in those other channels [11].

With the ever-increasing need for higher bit-rates, researchers questioned which is the fiber's maximum capacity. Using Shannon's information theory and extending it to the nonlinear propagation scheme presented in silica fiber a maximum theoretical capacity was proposed [17, 18, 19, 20]. A theoretical maximum capacity in a channel affected by additive white Gaussian noise can be written as [12]:

$$C = M_s \times B \times 2 \times \log_2(1 + SNR) \tag{2.1}$$

where M_s represents the number of different spatial paths available, B the system's bandwidth, the logarithmic term represents the maximum possible spectral efficiency (SE) of a single polarization and SNR is the signal-noise ratio. It is easily seen that the easiest way to increase capacity is to increase the number of spatial paths or to increase the bandwidth. Furthermore, the logarithm can also be increased but, due to the SE being already quite close to the Shannon limit, further increase only provides marginal gain [12].

Increasing the bandwidth has one major problem: in amplified links, the amplification bandwidth has to be at least the system's bandwidth, a current and active area of research [21]. Another active area of research is the use of several parallel spatial paths, usually called SDM [12]. This can be accomplished in three different ways, using already deployed parallel fibers, using several cores inside an optical fiber, constructing a fiber with several modes available, or a mix between these approaches, the latter two improving spatial density.

2.3. Space division multiplexing

This section presents a review of several options for SDM. In subsection 2.3.1 parallel fibers are introduced, followed by multimode fibers in subsection 2.3.2, and finally in subsection 2.3.3 multicore fibers are presented.

2.3.1. Parallel fibers

Using several parallel fibers is the oldest type of SDM [12], comprising of several distinct fibers transmitting different information. The main advantage of this type of SDM is that only one system has to be projected and then repeated for how many fibers the system composes, simplifying development and implementation [12]. However, the main disadvantage is the space required [12].

2.3.2. Multimode fiber

Besides the fundamental propagating mode, several others can propagate in a fiber core. How many and which modes propagate depend on the physical dimensions and differences in refractive indexes of core and cladding [11]. Thus, if different information propagates in different modes, a type of SDM is realized [22]. Multimode fibers and single-mode fibers have the same physical structure, shown in fig. 2.3. However, a bigger core diameter favors more modes to propagate [11]. Few-mode fibers are a subset of multimode fibers where only a subset of the fiber waveguide modes is used [22].

When several modes co-propagate, severe crosstalk (XT) exists between the different modes and, in some cases, complex multiple-input multiple-output (MIMO) and digital signal processing (DSP) are required [23].

Multimode fibers is an active area of investigation with increasingly different fibers [24, 25] and simulation models still being developed [26].

2.3.3. Multicore fiber
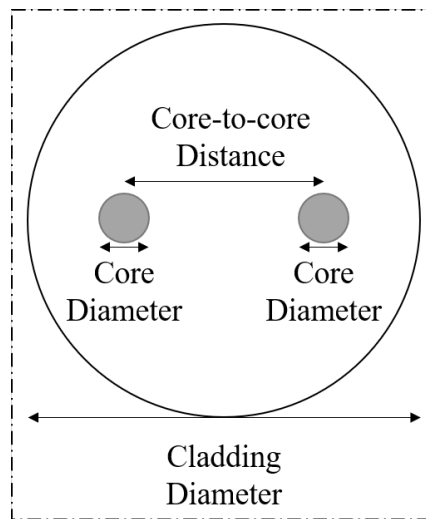
FIGURE 2.4. Multi-core fiber cross-section.

As stated above, one type of SDM is MCF and they come in several flavors. Fig. 2.4 shows a cross-section of a 2-core MCF. One possible distinction is between weakly-coupled and strongly-coupled cores. In a weakly-coupled MCF (WC-MCF), each core acts as an individual waveguide and the interference between neighboring cores is kept sufficiently low [23]. Furthermore, WC-MCF typically have a core-to-core distance higher than 30 µm and a coupling coefficient between neighboring cores lower than 10^{-2}/m. This arrangement sacrifices core density but MIMO DSP is not required for recovering the transmitted signal [12]. In strongly-coupled cores, high core-density is achieved by reducing the core-to-core distance, intentionally introducing interference between adjacent cores, with a

typical coupling coefficient between neighboring cores superior to 10^{-1}/m and a core-to-core distance inferior to 30 µm [23]. Furthermore, in strongly-coupled MCF, MIMO and DSP have to be employed to recover the transmitted signal, since this type of MCF can be considered a form of multimode fiber [23].

When optical power is launched only into the input of one core, the interfering core, of a WC-MCF, optical power is found at the output of that core and of the adjacent core, the interfered core [23]. This phenomenon is called ICXT, and the ICXT level is defined as the ratio between the power at the output of the interfered core and at the output of the interfering core [23].
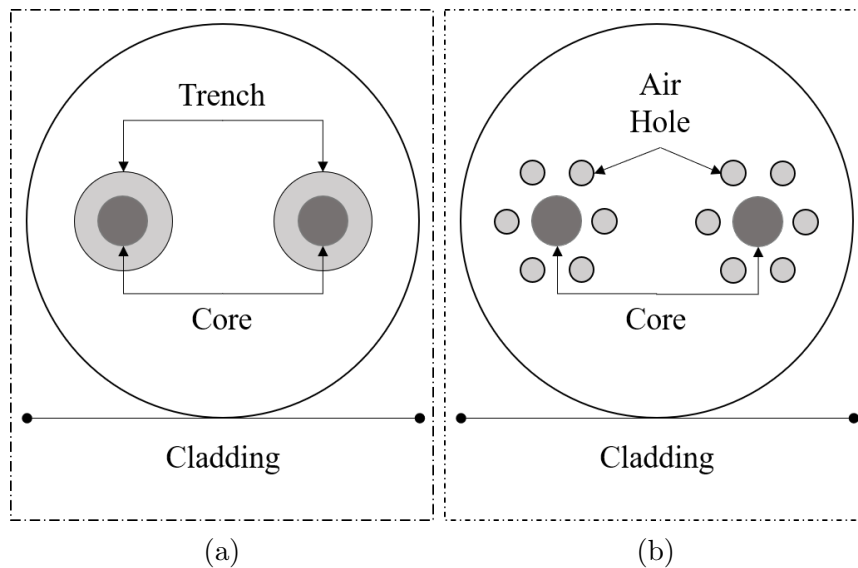
FIGURE 2.5. Trench assisted (a) and hole assisted (b) MCF cross-section.

To increase core density without increasing the interference between adjacent cores some suppression techniques were developed. Trench-assisted MCF consists of surrounding each core with a trench where the material refractive index is lower than the cladding refractive index [27, 28, 29]. Another proposed solution is to surround each core with holes, this aproach is called hole-assisted MCF [30, 31, 32]. Fig. 2.5 shows the cross-sections of a trench-assisted MCF and of a hole-assisted MCF.

With MCF having several cores, another distinction based on core type is possible. If all cores have similar effective refractive indexes, either single-mode core or multimode core, the MCF is called homogeneous [23]. If a mix of cores with different refractive indexed is used, then it's a heterogeneous fiber, reducing interference between adjacent cores [23].

Using the ICXT suppression techniques presented above and a multitude of core patterns, WC-MCF with up to 30 cores are possible [33]. High core density increases the cable capacity and improves the interconnects density addressing the capacity demands of DCs [34].

In WC-MCF the bend radius of the fiber is an important parameter to characterize ICXT [23]. A critical bending radius can be defined based on the fiber physical properties,

when the fiber bending radius is smaller than the critical radius large ICXT degradation occurs and on the opposite case the ICXT is dominated by statistical properties [23]. Considering a constant bending radius, the ICXT is modeled by introducing random phase shifts (RPS) at random phase matching points located longitudinally through the MCF's length [35]. If a large number of RPS is considered then the real and imaginary parts of the ICXT field have a Gaussian profile [35], a characteristic used to assess if the model is correctly implemented in the numerical simulator.

To capture the stochastic properties of the ICXT, its power can be measured in a short time duration where the transmission conditions are assumed to be constant. This power measurement usually called short-time average crosstalk (STAXT), measured in a time fraction, $\mathcal{T}$, has a duration of 100 to 200 ms when experimentally measured [36, 37]. The STAXT measured as the mean power of the ICXT field in a time fraction helps to characterize the stochastic nature of the ICXT and is defined by [38]:

$$STAXT_n(t) = \frac{1}{\mathcal{T}} \int_{t-\mathcal{T}}^{t} |E_{ICXT}|^2(\tau) \mathrm{d}\tau \qquad (2.2)$$

where n is the n-th time fraction where the ICXT power is being measured and $E_{ICXT}(t)$ is the ICXT field .

Because of the stochastic properties of the ICXT, the system using MCF can occasionally become inoperative due to the degradation induced by the ICXT [39]. Outage probability has been used to quantify these extreme events that render the system inoperable [40].

2.4. Optical receivers

In fiber optic communications, there are two main types of signal detection: direct and coherent.

DD with intensity modulation explores only one degree of freedom, it uses a photo-detector to convert the optical signal to an electrical signal. Symbol decision is performed on the amplitude of the electric signal. This contributes to simple and low spectral efficient systems [11].

There are two main types of photo-detector, avalanche (APD) and p-i-n photo-diodes [11]. The p-i-n photo-diode consists of a p-n junction with an intrinsic material between the p-n junction. The photo-diodes are reverse-biased and their characteristics, such as responsivity and bandwidth, are defined by the intrinsic material used. Responsivity relates the electric current to the optical power incident on the photo-detector and the bandwidth is determined by the speed at which the photo-detector material responds to changing incident optical power [11]. However, all photo-detectors known require a small amount of current to reliably operate, which ultimately translates to minimum optical power requirements [11].

APDs were designed with an internal structure capable of providing an amplification gain. These photo-diodes follow the p-i-n structure but a new p-layer is added. This new layer is called the multiplication layer and it is responsible for boosting the current generated in the photo-diode. For this reason, APDs are used in systems with low received power, a normal use case is in DCs [41].

As CD is nonlinear in intensity modulation DD systems, simple electronic CD compensation in the receiver is not efficient [4]. However, other CD compensation techniques are available but they are less flexible than electronic CD compensation [4].
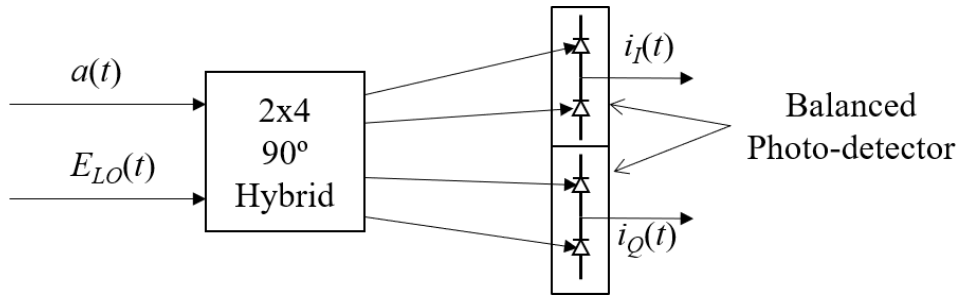
FIGURE 2.6. Coherent receiver with balanced photo-detector.

Coherent receivers are a step forward in using high bit-rate, high spectral efficiency advanced modulation schemes [4]. A big advantage compared to DD is the use of polarization diversity and both phase and quadrature components independently [42]. Furthermore, using DSP to compensate for several transmission effects is possible [4]. A typical implementation of coherent-detection uses balanced photo-detection, detecting two signals to eliminate signal-to-signal beat noise (SSBN) component introduced by square-law detection of the optical signal [43]. Moreover, it uses a local oscillator, two photo-detectors pairs per signal component, one 90$^\text{o}$ hybrid per polarization and a DSP with algorithms for transmission impairments compensation. Fig. 2.6 shows a block digram of a coherent receiver where the incoming optical signal, $a(t)$, is interfered with the local laser, $E_{LO}(t)$, using a 90$^\text{o}$ hybrid composed of optical couplers and a polarization beam splitter [42]. At the hybrid output, after the signal is detected using balanced photo-detection, its in-phase, $i_I(t)$, and quadrature, $i_Q(t)$, components can be digitized and DSP can be applied for transmission impairments compensation. These DSP algorithms consume a great deal of power, cooling, cost and packaging can also be a challenge in DCs since space and airflow are both limited [4].

Square-law detection of the optical signal at the input of the photo-detector, $b(t)$, produces a photo-current proportional to [43]:

$$\mid b(t) \mid^2 = 2A\Re\{E_s(t)\} + \mid E_s(t) \mid^2 + A^2 \tag{2.3}$$

where $b(t) = A + E_s(t)$, A represents the continuous wave (CW) component and $E_s(t)$ is the information bearing signal. The objective is to recover the first term on the right hand side of the equality, the second term is called SSBN and, the last term is a known quantity

that does not hinder information signal recovery. Besides balanced photo-detection other SSBN mitigation techniques are available. One consists of using a CW much larger than the information signal [44, 45], this technique is not convenient due to the power constraints posed in DCs, another is the use of a guard band between CW and the information signal wasting bandwidth [46].

Furthermore, an alternative to coherent detection and compatible with DD is Stokes vector detection [4]. This method increases the degrees of freedom available in DD for signal multiplexing using intensity modulation for both polarizations and inter-polarization differential phase. However, this system needs an DSP and a complex detection setup for correct information retrieval [4].

Another possible alternative to coherent detection compatible with DD is KK receivers. These receivers make it possible to recover complex-valued signal from the photo-current generated by the photo-detector and eliminate the SSBN component [43]. However, the transmitted signal has to be a single-sideband (SSB) signal and the waveform has to be minimum-phase [47]. If the minimum-phase condition is met, the absolute value of the signal and it's phase are uniquely related by the Hilbert transform making it possible to recover a complex-valued signal [47].

An SSB signal is defined as any complex-valued signal where its spectrum is located to one side of an arbitrary reference frequency marked by a CW component added in the transmitter [43]. Furthermore, to fulfill the minimum phase condition the signal's peak-to-average power ratio, $PAPR$, given by [48]:

$$PAPR = \frac{\max(|E_s(t)|^2)}{\overline{|E_s(t)|^2}} \tag{2.4}$$

where $E_s(t)$ is the information bearing signal, $\max(x)$ gives the maximum value of x and $\overline{x}$ gives the average of x, has to be larger than the carrier-to-signal power ratio, $CSPR$, given by [48]:

$$CSPR = \frac{\overline{|A|^2}}{\overline{|E_s(t)|^2}}. \tag{2.5}$$

With the minimum phase condition fulfilled it is possible to recover a complex-valued signal using the following algorithm [47]:

$$s(t) = \sqrt{i(t)}e^{j\mathcal{H}\left\{\log\left(\sqrt{i(t)}\right)\right\}} \tag{2.6}$$

where $\log(x)$ is the natural logarithm of x, $\mathcal{H}\{u(t)\}$ is the Hilbert transform of $u(t)$ given by $\mathcal{H}\{u(t)\} = \frac{1}{\pi}p.v. \int_{-\infty}^{\infty} \frac{u(\tau)}{t-\tau} \, d\tau$, and $i(t)$ is the photo-current.

Fig. 2.7 shows a block diagram of the ideal KK algorithm. The photo-current, $i(t)$, can be digitized and the remaining operations implemented in the digital domain.

When compared to other options this algorithm presents several advantages such as low cost, high spectral efficiency, low power consumption and high reconstruction accuracy [43]. Polarization multiplexing is possible but the technology of today is still too
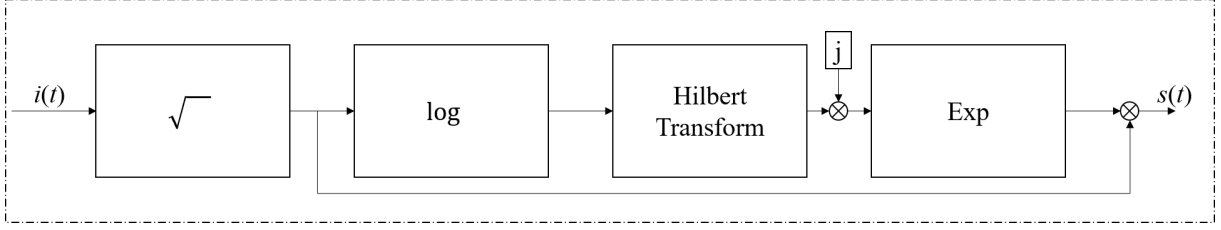
FIGURE 2.7. KK receiver block diagram.

lavish to be employed in DCs [43]. However, the logarithm function introduces spectral broadening requiring enough bandwidth when the algorithm is applied in a DSP. This usually needs digital up-sampling of the photo-current to accommodate the spectral broadening [47]. Another problem presented by the KK algorithm is the need for the ADC to digitize the information bearing signal and the strong carrier, with the ADC having to accommodate the dynamic range of the photo-detected signal [49]. In addition, due to the nonlinear functions used in the KK algorithm, the noise present in the photo-current can be amplified when the signal is close to zero requiring higher CSPR values to prevent noise amplification [50].

To relax the ADC requirements AC coupled photo-detection can be employed. However, the KK algorithm requires that the average component, eliminated in the AC coupling, must be re-introduced digitally [49]. A method to estimate the signal average component based on spectral analysis of the reconstructed signal is proposed in [49]. This method introduces a DC_{metric} based on a power level within a guard band introduced between the information bearing signal and the optical carrier. This method works because the error between the introduced bias and the correct bias is proportional to the signal in the guard band [49]. The proposed DC_{metric} is given by [49]:

$$DC_{metric} = \frac{B_{norm}^2}{B_{GB}^2} \frac{\int_0^{f_{GB}} |r_{KK}(f)|^2 \mathrm{d}f}{\int_{f_{norm}}^{f_{norm}+B_{norm}} |r_{KK}(f)|^2 \mathrm{d}f} \qquad (2.7)$$

where B_{GB} is the guard band (starting at 0 Hz to f_{GB}), B_{norm} is the bandwidth from $f_{norm} > f_{GB}$ to $f_{norm} + B_{norm} < f_{GB} + 2B$, B being the bandwidth of the information bearing signal and $r_{KK}(f)$ is the Fourier transform of the reconstructed signal given by eq. 2.6.
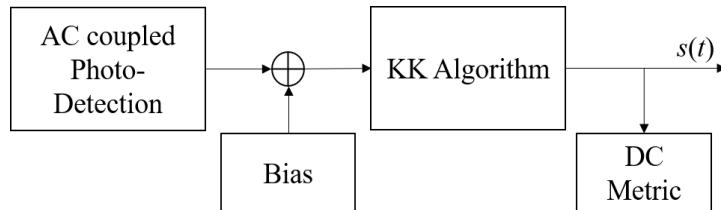
FIGURE 2.8. AC coupled KK algorithm block diagram.

Fig. 2.8 shows a block diagram of the optical receiver when the AC coupled KK algorithm is used. The incoming optical signal is photo-detected, AC coupled and digitized.

The digital signal is normalized to unitary power, the bias is introduced and the KK algorithm applied. The DC_{metric} is used to assess if the added bias is correct.

To prevent the KK algorithm from amplifying the noise introduced by the receiver when the signal is close to zero, two steps are taken to reduce noise [50]. Before the logarithm, the photo-current is be clipped to a high minimum value (a percentage of the mean's signal value), then the spectrum of the output of the logarithm is restricted.
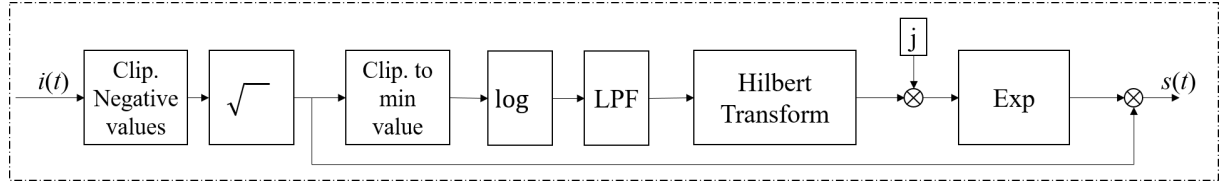
FIGURE 2.9. Clipping enhanced KK algorithm block diagram.

Fig. 2.9 shows a block diagram of the clipping enhanced KK receiver. The negative values of the photo-current are clipped to zero and the square root is applied to the signal. Then the waveform is clipped to a minimum value, the natural logarithm function is applied and a low pass filter (LPF) is used to reduce noise, the remaining part of the algorithm is equal to the ideal KK algorithm, the Hilbert transform is applied and a complex-valued signal is computed.

Some experiences using KK receivers were successfully performed, a 7.9 km long 37-core MCF with 99 WDM channels per core was able to transmit 16-QAM and 64-QAM signals, both using polarization division multiplexing (PDM) and a KK receiver [51], and a 30 km long 3-mode, few-mode fiber was used to successfully transmit a PDM-16-QAM signal using KK receivers and a 6×6 MIMO to undo the modal crosstalk introduced by the few-mode fiber [52].

CHAPTER 3

System model

In this chapter, the system description is presented in section 3.1, with the following sections comprising a detailed description of all the blocks in the system. Section 3.2 presents the transmitter model, section 3.3 the fiber model and, finally, section 3.4 the receiver model. Section 3.5 shows the metrics used to characterize the system performance and in section 3.6 it is shown that the blocks presented were correctly implemented in the numerical simulator.

3.1. System description
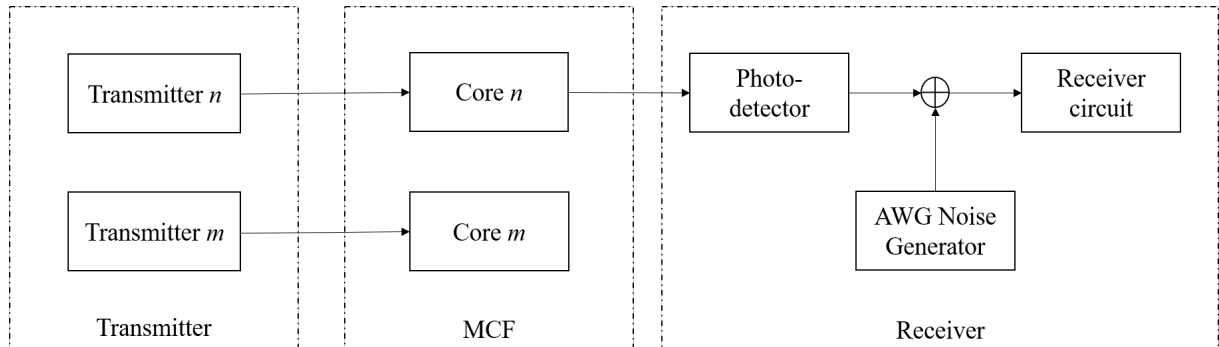
FIGURE 3.1. System design overview.

The system comprises three main blocks. The first block contains two transmitters, one for each fiber core, the second block represents the multicore fiber with two weakly-coupled cores, the third and final block comprises all the receiver apparatus for detecting the received signal. The MCF introduces ICXT through the entire length of the fiber degrading the signal, and the receiver introduces electrical noise modeled as additive white Gaussian (AWG) noise.

The received signal quality and system performance can be assessed using several metrics such as bit error rate (BER), EVM and outage probability. Fig. 3.1 represents a general model of the system. However, some differences can be present depending if it is deployed in inter-data-center or intra-data-center links.

The following sections detail all the blocks presented in fig. 3.1.
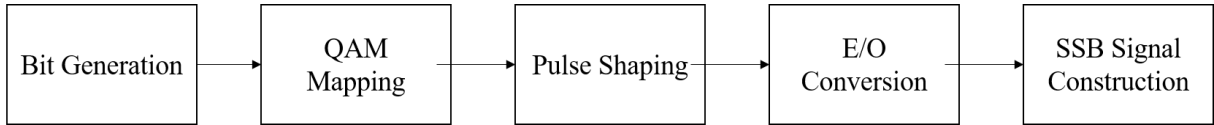
FIGURE 3.2. Transmitter model block diagram.

3.2. Transmitter model

The function of the transmitter is to convert the electrical bits to optical symbols. As seen in fig. 3.2, the transmitter has several functions. The bits are mapped, using Gray mapping, to a 16-QAM square constellation. Then, a root-raised cosine (RRC) pulse shape is imposed. A linearised IQ modulator is used next to perform the conversion to an optical signal. Finally, by adding a CW component to the left of the information bearing signal's spectrum, an SSB signal is formed.

As in [53, 54], a FEC is used with 7% overhead that grants an output BER after decoding of $< 10^{-15}$ if the BER before decoding is $\leq 4.5 \times 10^{-3}$ [55]. The system operates at a bit rate of 214 Gbit/s, including FEC, and has a symbol rate, R_s, of $R_s = 53.5$ GBd.

3.2.1. Pulse shaping

The transmitter imposes an RRC pulse shape in the signal after the bits are mapped to the constellation and before electro-optical conversion. In the receiver, a matched filter is employed maximizing the signal-to-noise ratio [20]. This arrangement makes the signal at the input of the decision circuit at the receiver have a raised cosine (RC) shape, eliminating symbolic interference at the optimal sampling time [20, 56]. The RC filter transfer function, $S_c(f)$, is given by [20, 56]:

$$S_c(f) = \begin{cases} T_s, & |f| \leq \frac{1-\beta_r}{2T_s} \\ T_s \cos^2\left[\frac{\pi T_s}{2\beta_r}\left(|f| - \frac{1-\beta_r}{2T_s}\right)\right], & \frac{1-\beta_r}{2T_s} < |f| < \frac{1+\beta_r}{2T_s} \\ 0, & \text{otherwise} \end{cases} \tag{3.1}$$

where β_r is the roll-off factor and T_s is the symbol period given by $\frac{1}{R_s}$. To accomplish an RRC filter its transfer function is given by $\sqrt{S_c(f)}$ where $S_c(f)$ is given by eq. 3.1.

Fig. 3.3 represents the electrical RRC shaped signal spectrum at the transmitter. The signal has a bandwidth of 27 GHz since the RRC filter has a roll-off factor of 0.01.

3.2.2. Electro-optical conversion

For electro-optical conversion of the signal, an IQ modulator was used. The IQ modulator can be comprised of two Mach-Zhender modulators (MZM), one for the phase component and another for the quadrature component of the QAM signal, and a phase modulator

16
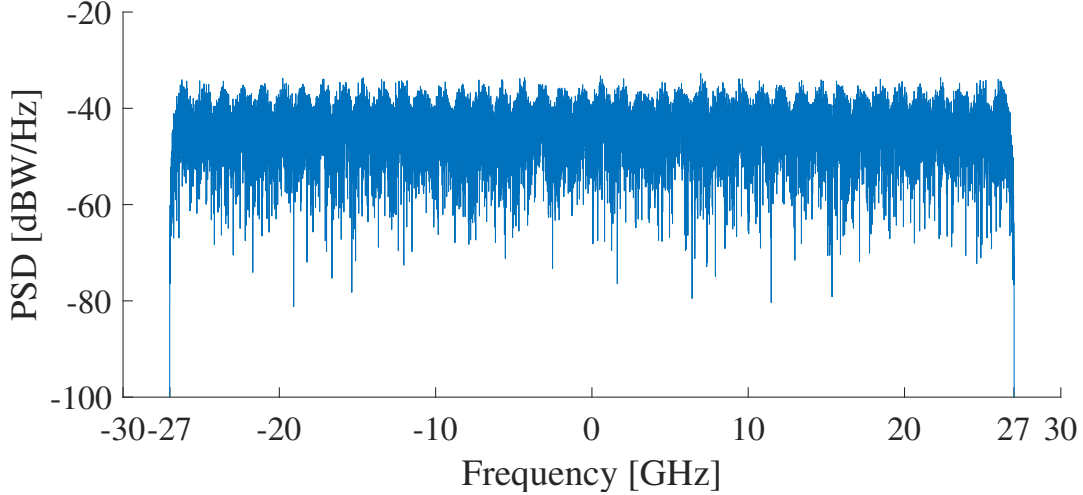
FIGURE 3.3. RRC signal spectrum.

that introduces a phase shift of $\frac{\pi}{2}$ between the signals [42]. Each MZM, $e_{out,comp}(t)$, is given by [42]:

$$e_{out,comp}(t) = \cos\left(\frac{\pi}{2V_{sv}}\left(v_{comp}(t) + V_{bias,MZM}\right)\right) \qquad (3.2)$$

where $e_{out,comp}(t)$ is the output of the MZM, $comp \in \{I, Q\}$ corresponds to one of the QAM components, phase or quadrature; V_{sv} is the switching voltage; $V_{bias,MZM}$ is the bias point of the MZM; and $v_{comp}(t)$ is the driving signal for the corresponding phase or quadrature component of the QAM signal. The MZMs operate at the minimum bias point, $V_{bias,MZM} = -V_{sv}$, and are linearised at this point to avoid the introduction of non-linear effects. The MZM linearised at the minimum bias point, $e_{lin,comp}(t)$, is given by:

$$e_{lin,comp}(t) = \frac{\pi}{2V_{sv}}v_{comp}(t) \qquad (3.3)$$

Using a nonlinearised MZM it is still possible to achieve a square constellation at the output of the MZM, however, the driving signal has to compensate for the MZM's non-linearity [57]. The IQ modulator, $e_{out}(t)$, is given by [42]:

$$\frac{e_{out}(t)}{e_{in}(t)} = \frac{1}{2}e_{lin,I}(t) + \jmath\frac{1}{2}e_{lin,Q}(t) \qquad (3.4)$$

where $e_{out}(t)$ and $e_{in}(t)$ are the output and input of the IQ modulator, respectively; $e_{lin,I}(t)$ is given by eq. 3.3 when the phase component of the QAM signal is used, and similarly, $e_{lin,Q}(t)$ is given by eq. 3.3 when the quadrature component of the QAM signal is used.

Fig. 3.4 shows the optical signal spectrum after electro-optical conversion. The RRC signal is converted to an optical signal using the aforementioned IQ modulator with a switching voltage of 4 V. The signal has a bandwidth of 54 GHz and an optical power of
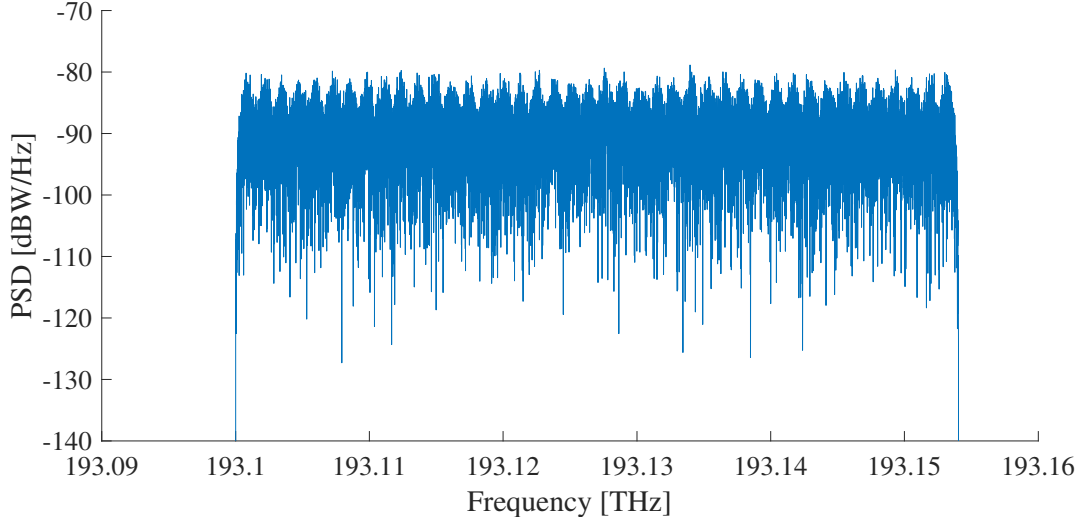
FIGURE 3.4. Spectrum of the QAM signal after electrical-optical conversion.

-16.1 dBm.

3.2.3. SSB signal construction

An SSB signal is an optical signal where the information bearing signal's spectrum is located to one side of an arbitrary frequency [43] to which a non-zero CW component, A, is added. The SSB signal, $E_{SSB}(t)$, can be written as:

$$E_{SSB}(t) = \sqrt{P_c}\left(A + E_s(t)\right) \tag{3.5}$$

where P_c is the optical power of the signal launched to the fiber core and $E_s(t)$ is the information bearing signal given by:

$$E_s(t) = \sum_{k=-\infty}^{+\infty} a_k h_{RRC}(t - kT_s) \tag{3.6}$$

where a_k is the optical complex amplitude of the k-th transmitted symbol and $h_{RRC}(t)$ is the RRC impulse response given by $\mathfrak{F}^{-1}\left\{\sqrt{S_c(f)}\right\}$ where $\mathfrak{F}^{-1}\left\{U\left(f\right)\right\}$ is the inverse Fourier transform of $U\left(f\right)$ and $S_c\left(f\right)$ is given by eq. 3.1.

The optical carrier power is adjusted, changing the CSPR to the required value in the SSB signal.

Fig. 3.5 shows the spectrum of the SSB signal at the output of the transmitter before being launched into the fiber core. The optical signal has a power of 0 dBm where the information bearing signal has -16.1 dBm and the CW component has -0.1 dBm. Furthermore, the signal has a PAPR of 7.9 dB and a CSPR of 16 dB. No gap was considered between the information bearing signal and the CW component.
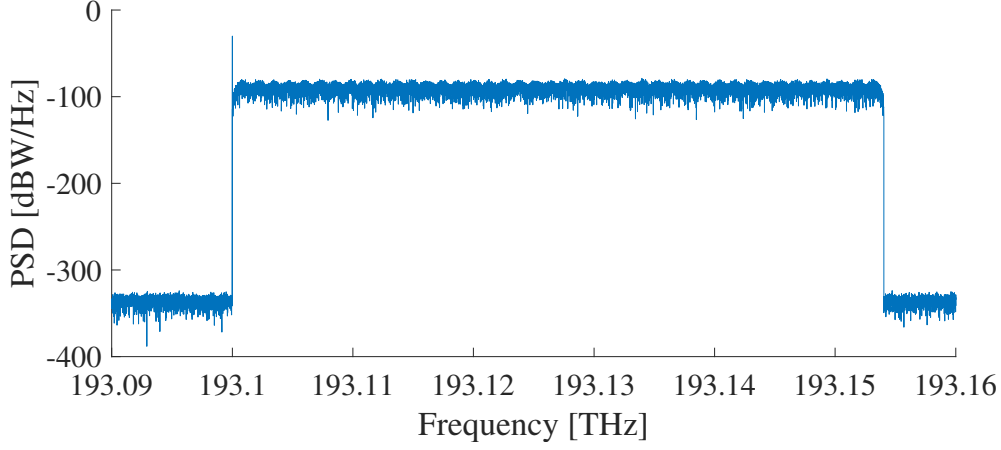
FIGURE 3.5. Spectrum of the SSB signal.

3.3. Fiber model
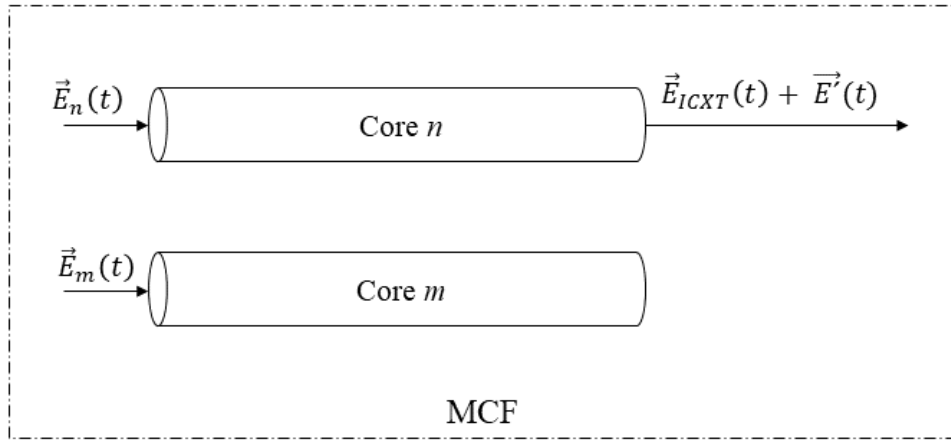
FIGURE 3.6. Two core weakly-coupled fiber model.

The SSB signal is launched to a two core WC-MCF represented by fig. 3.6 where the output of the test core is composed by the signal launched to the test core and the interfering field generated by the interfering core. The test core, core n, is the one where the information-bearing signal propagates, core m is the interfering core. The signal launched to the test core, $\overrightarrow{E}_n(t)$, is given by:

$$\overrightarrow{E}_n(t) = E_{n,x}(t) \; \hat{x} + E_{n,y}(t) \; \hat{y} \tag{3.7}$$

where $E_{n,pol}(t) = E_{n,x}(t) = E_{n,y}(t) = \frac{1}{\sqrt{2}} E_{SSB}(t)$ with $E_{SSB}(t)$ given by eq. 3.5 and $pol \in \{x, y\}$ representing each polarization that composes the signal. Similarly, the signal launched into the interfering core, $\overrightarrow{E}_m(t)$, can be written as:

$$\overrightarrow{E}_m(t) = E_{m,x}(t) \; \hat{x} + E_{m,y}(t) \; \hat{y} \tag{3.8}$$

where $E_{m,pol}(t) = E_{m,x}(t) = E_{m,y}(t) = \frac{1}{\sqrt{2}} E_{SSB}(t)$. Furthermore, the signals $E_{n,pol}(t)$ and $E_{m,pol}(t)$ are uncorrelated since the symbol streams that give them origin are uncorrelated.

The ICXT complex envelope at the output of the test core, $\overrightarrow{E}_{ICXT}(t)$, can be written as follows [38]:

$$\overrightarrow{E}_{ICXT}(t) = E_{ICXT,x}(t)\,\hat{x} + E_{ICXT,y}(t)\,\hat{y} \tag{3.9}$$

with the ICXT field components given by [58, 38]:

$$E_{ICXT,x}(t) = \mathfrak{F}^{-1}\{E_{m,x}(\omega)F_{x,x}(\omega)\} + \mathfrak{F}^{-1}\{E_{m,y}(\omega)F_{y,x}(\omega)\} \tag{3.10}$$

$$E_{ICXT,y}(t) = \mathfrak{F}^{-1}\{E_{m,x}(\omega)F_{x,y}(\omega)\} + \mathfrak{F}^{-1}\{E_{m,y}(\omega)F_{y,y}(\omega)\} \tag{3.11}$$

where ω is the angular frequency and the transfer functions $F_{b,pol}(\omega)$, that model the ICXT from the input of core m to the output of core n, are given by [38, 58]:

$$F_{b,pol}(\omega) = -\jmath\frac{\overline{K}_{nm}}{\sqrt{2}}e^{-\jmath\overline{\beta}_n(\omega)L}\sum_{k=1}^{N}e^{-\jmath\Delta\overline{\beta}_{mn}(\omega)z_k}e^{-\jmath\phi_{b,pol}^{(k)}} \tag{3.12}$$

where $b \in \{x,y\}$ represents the different polarizations from core m, $\overline{K}_{nm}$ is the coupling coefficient, which is related to fiber physical properties and can be obtained from the ICXT level using $X_c = N|\overline{K}_{nm}|^2P_m/P_n$ with P_m and P_n being, respectively, the power in the interfering and test core [38], $\overline{\beta}_n$ is the average of the intrinsic propagation constants of the two polarization directions of core n and takes into account the group velocity delay (GVD) effects and propagation delay, L is the WC-MCF length, N is the number of RPS, z_k is the k-th random coordinate uniformly distributed between $(k-1)L/N$ and kL/N, $\phi_{b,pol}^{(k)}$ is the k-th RPS introduced at z_k and is uniformly distributed between 0 and 2π, finally $\Delta\overline{\beta}_{mn}(\omega)$ is given by [59]:

$$\Delta\overline{\beta}_{mn}(\omega) = \Delta\overline{\beta}_{0,mn} + d_{mn}\omega - \frac{\Delta D_{mn}\lambda^2\omega^2}{4\pi c} \tag{3.13}$$

where $\Delta\overline{\beta}_{0,mn}$ is the difference of the propagation constants at $\omega = 0$, d_{mn} is the average walkoff parameter between the cores m and n, and is related to the skew between cores, S_{mn}, by $d_{mn} = S_{mn}/L$, ΔD_{mn} is the difference between dispersion parameters of core m and core n, λ is the optical carrier wavelength, and c is the speed of light in a vacuum.

The optical field at the output of the test core considering GVD and random polarization rotation due to birefringence in core n, $\overrightarrow{E}'(t)$, is given by:

$$\overrightarrow{E}'(t) = E_x'(t)\hat{x} + E_y'(t)\hat{y} \tag{3.14}$$

where $E_x'(t)$ and $E_y'(t)$ are given by [60]:

$$E_x'(t) = [e^{\jmath\theta}\cos(\Gamma)E_{n,x}(t) - e^{-\jmath\psi}\sin(\Gamma)E_{n,y}(t)] * \mathfrak{F}^{-1}\{e^{-\jmath\overline{\beta}_n(\omega)L}\} \tag{3.15}$$

$$E_y'(t) = [e^{\jmath\psi}\sin(\Gamma)E_{n,x}(t) + e^{-\jmath\theta}\cos(\Gamma)E_{n,y}(t)] * \mathfrak{F}^{-1}\{e^{-\jmath\overline{\beta}_n(\omega)L}\} \tag{3.16}$$

where ψ, θ, and Γ are random processes that can be assumed constant along a time fraction and are uniformly distributed between 0 and 2π.

If more than one interfering core is considered, the ICXT field is composed of the sum of the ICXT field contributions of each interfering core [38, 58]. As a result of uncorrelated data sequences and RPS, these contributions are independent. In addition, if the interfering cores all have the same parameters, then the ICXT level is given by $X_c = N_c N |\overline{K}_{nm}|^2 P_m / P_n$, where N_c is the number of interfering cores and the ICXT field associated with each interfering core is given by eq. 3.9.

3.4. Receiver model

Photo-Detection	→	KK Algorithm	→	Dispersion Compensation	→	Matched Filter	→	Symbol Sample and Decision
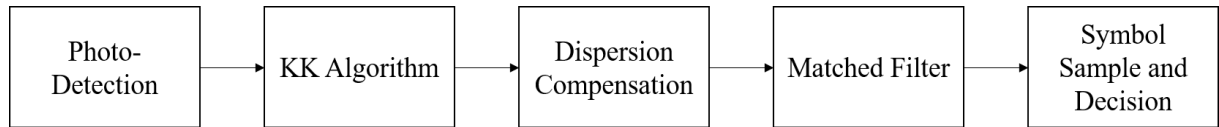
FIGURE 3.7. Receiver model.

The receiver is composed of several stages, as shown in fig. 3.7. The incoming optical signal is detected, followed by a possible digitalization stage, after that, the KK algorithm is applied, recovering both components of the QAM signal, phase and quadrature, subsequently, dispersion compensation, matched filtering and symbol decision can be applied.

The impinging optical signal composed by the optical field at the output of the test core, $\overrightarrow{E}_{ICXT}(t) + \overrightarrow{E}'(t)$, is photo-detected by a p-i-n photo-diode giving:

$$i(t) = R_\lambda(|E'_x(t) + E_{ICXT,x}(t)|^2 + |E'_y(t) + E_{ICXT,y}(t)|^2) + n(t) \qquad (3.17)$$

where R_λ is the p-i-n's responsivity [11], $E'_x(t)$ and $E'_y(t)$ are the field components of the signal at the output of the test core without ICXT given by eq. 3.15 and by eq. 3.16, respectively. $E_{ICXT,x}(t)$ and $E_{ICXT,y}(t)$ are the ICXT field components generated by the interfering core given by eq. 3.10 and by eq. 3.11, respectively, and $n(t)$ is electrical noise with thermal noise being the main component modelled as AWG noise with variance given by [11]:

$$\sigma_c^2 = R_\lambda^2 NEP^2 B_{e,n} \qquad (3.18)$$

where NEP is the noise-equivalent power [11] and $B_{e,n}$ is the equivalent noise bandwidth, defined as $B_{e,n} = \int_0^{+\infty} \left| \frac{H_R(f)}{H_R(0)} \right|^2 df$, where $H_R(f)$ is the receiver filter transfer function.

3.4.1. Ideal KK algorithm

After using the ideal KK algorithm on the photo-detected signal, the resulting signal given by eq. 2.6 is show in the following figures.
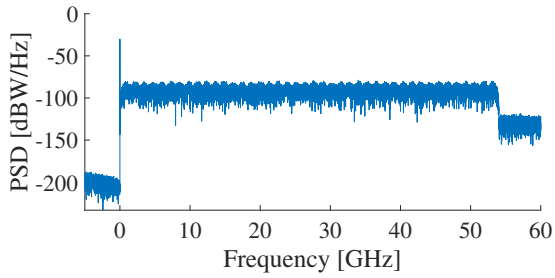
(a) Signal spectrum after ideal KK algorithm.
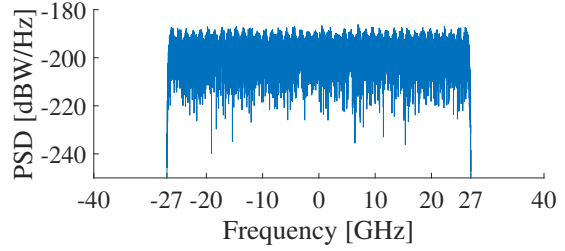
(b) Signal spectrum after ideal KK algorithm and matched filtering.

FIGURE 3.8. Received signal after the ideal KK algorithm in back-to-back operation.

Fig. 3.8 presents the signal obtained in back-to-back operation after the ideal KK algorithm is applied at different stages in the receiver. The signal at the output of the transmitter is shown in fig. 3.5, and at the receiver electrical noise is considered. Fig. 3.8a shows the signal immediately after the ideal KK algorithm, eq. 2.6. The signal immediately after the ideal KK algorithm is an SSB signal with a bandwidth of 54 GHz since all the spectrum of the QAM signal is located to one side of 0 Hz because the optical carrier marks the zero frequency after the ideal KK algorithm is applied. To recover a QAM signal, the signal immediately after the ideal KK algorithm has a spectral shift of $e^{-j2\pi B_{RRC}t}$ applied to it, where B_{RRC} is the bandwidth of the RRC signal, after which the matched filter can be applied giving origin to the RC shape signal seen in fig. 3.8b. At this point symbol sampling and symbol decision can be performed.

3.4.2. AC coupled KK algorithm

A problem presented by the KK algorithm is the need to digitize the incoming signal with the signal's average component, thus increasing the required dynamic range of the ADC. Using AC coupled detection where the bias of the photo-detected signal is eliminated and re-introduced after digitalisation would solve this problem. However, to verify if the introduced bias is correct, the metric presented in eq. 2.7 is used, although it requires a guard band between the optical carrier and the information bearing signal.

Fig. 3.9 shows the spectrum of the optical signal compatible with this algorithm. The optical signal has a CSPR of 16 dB and an optical power of 0 dBm, the optical carrier has a power of -0.1 dBm and the information- bearing signal a power of -16.1 dBm. This signal is similar to the one already presented in fig. 3.5. However, a guard band between the optical carrier and the information-bearing signal was introduced with 10% of the symbol rate of the QAM signal, 5.35 GHz, as in [49].

Fig. 3.10 shows the received signal spectrum immediately after the KK algorithm is applied and after matched filtering is employed. The signal is obtained in back-to-back operation considering only electrical noise at the receiver. The transmitted signal
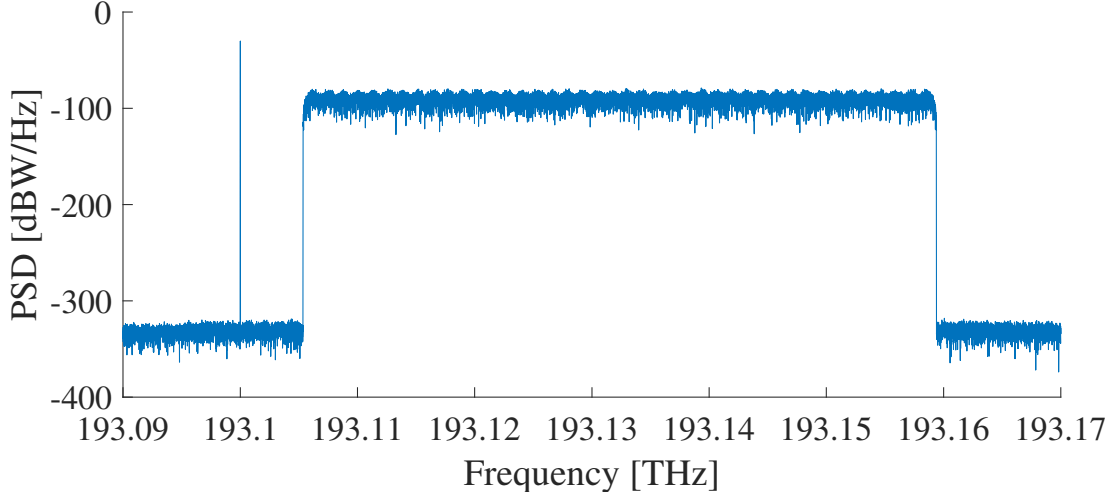
FIGURE 3.9. SSB signal spectrum with a guard band of 5.35 GHz, an optical power of 0 dBm and a CSPR of 16 dB.

(a) Signal spectrum with ideal bias added.

(b) Signal spectrum after ideal bias added and matched filtering.
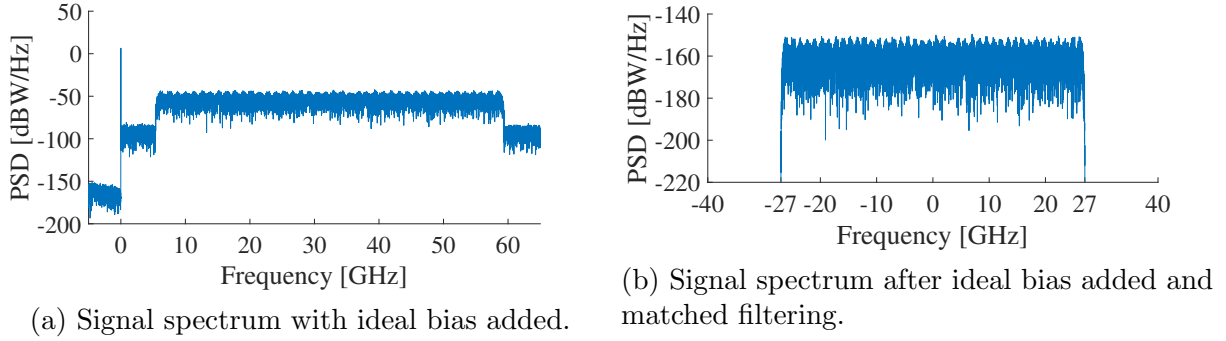
FIGURE 3.10. Received signal after the AC coupled KK algorithm in back-to-back operation.

is presented in fig. 3.9 and has a PAPR of 7.9 dB. The signal is photo-detected and AC coupled, after which the signal is normalized to unitary power and the ideal bias is added to the signal.

The ideal bias corresponds to where the metric, eq. 2.7, is at a minimum. To obtain the ideal bias, the metric is computed for several different biases until a minimum is found, having obtained an ideal bias for a set of symbols the search for the next set is restricted to 0.1 V in the vicinity of the previous ideal bias and only expanded if a minimum is not found in that region. Fig. 3.10a shows the signal spectrum immediately after the KK algorithm is applied. The signal is SSB and the guard band between the information bearing signal and the optical carrier is still present. To recover the QAM signal, a spectral shift of $e^{-j2\pi(B_{RRC}+B_{GB})t}$ is applied after which the matched filter can be employed yielding the RC shaped signal in fig. 3.10b. At this point, symbol sampling and symbol decision can be performed.

3.4.3. Clipping enhanced KK algorithm

The clipping enhanced KK algorithm works by clipping the low values of the waveform to a predetermined defined level. This predetermined level is normalized to the mean value of the photo-current and is given by [50]:

$$Normalized\ clipping\ level = \frac{Clipping\ level}{|i(t)|} \tag{3.19}$$

where $i(t)$ is given by eq. 3.17 and the *Clipping level* is the value to which the waveform is clipped.

The transmitted optical signal has no guard band between the optical carrier and the information-bearing signal. The signal's processing at the receiver, after the clipping enhanced KK algorithm is applied, is equal to the processing performed for the ideal KK algorithm.
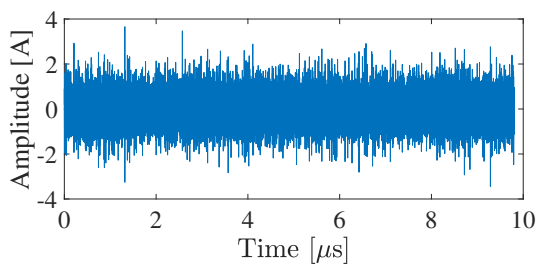
(a) Waveform after the Hilbert transform using an ideal KK algorithm.
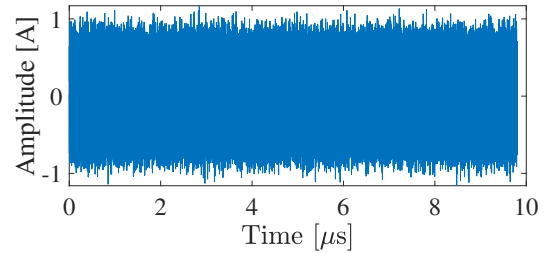
(b) Waveform after the Hilbert transform using a clipping enhanced KK algorithm with a normalized clipping level of $10^{-0.7}$.

FIGURE 3.11. Waveform after the Hilbert transform using a 45 km long SMF with a CSPR of 10 dB.

Fig. 3.11 shows two waveforms at the output of the Hilbert transform when using the ideal KK algorithm and the clipping enhanced KK algorithm for the received signal. The transmitted signal has an optical power of 0 dBm, a CSPR of 10 dB and 2^{19} symbols with a PAPR of 9.2 dB. The clipping level of the clipping enhanced KK algorithm was optimized to a 45 km long SMF, for more details see subsection 3.6.4.

From fig. 3.11a it is possible to see that the waveform has several peaks. These peaks cause large fast phase modulation at the output of the receiver. As the points where the photo-current approaches zero are stretched by the logarithm present in the KK algorithm they become large variations at the output of the Hilbert transform [50]. However, if these points near zero are clipped, these peaks do occur as seen in fig. 3.11b. The absence of peaks ensures a better performance of the clipping enhanced KK algorithm when compared to the ideal KK algorithm.

3.5. Performance assessment

The system performance can be assessed using several metrics, such as error vector magnitude, bit error rate and outage probability which are described in the following subsections.

3.5.1. Error vector magnitude

One way to assess the signal's quality is to calculate the EVM defined as the root-mean-square (RMS) value of the difference between the set of measured symbols after matched filtering and the ideal symbols [61]. This metric quantifies how much the received symbol differs from the sent symbol and is given by [61]:

$$EVM_{RMS} = \sqrt{\frac{\sum_{k=1}^{N_s} \left| s_0[k] - s_i[k] \right|^2}{\sum_{k=1}^{N_s} \left| s_i[k] \right|^2}} \qquad (3.20)$$

where N_s is the total number of symbols in the sequence, $s_0[k]$ is the normalized complex amplitude of the k-th received symbol and $s_i[k]$ is the normalized complex amplitude of the k-th symbol of the ideal constellation.

One effect that can degrade substantially the EVM without the signal being degraded is the signal's constellation rotation, which contributes to a higher EVM. To compensate for this effect, the EVM is calculated for each rotation of the constellation by $1^{\underline{o}}$ between $0^{\underline{o}}$ and $360^{\underline{o}}$. The effect is considered compensated for the minimum EVM calculated.

3.5.2. Bit error rate

BER is another metric that can be used to assess the quality of the received signal. It can be calculated using EVM by [61, 62]:

$$BER_{M-QAM} = \frac{2}{\log_2 M} \left(1 - \frac{1}{\sqrt{M}} \right) \text{erfc} \left(\sqrt{\frac{3 \log_2 \sqrt{M}}{(M-1) \log_2 M} \frac{1}{|EVM|^2}} \right) \qquad (3.21)$$

where the M is the modulation order of the QAM signal given by $M = 2^n$ with n being an integer, $\text{erfc}(x)$ is the complementary error function of x and EVM is given by eq. 3.20. Eq. 3.21 assumes a Gaussian noise channel and a perfectly sampled signal without inter-symbolic interference.

Direct error count is the most direct way of assessing the BER using Monte Carlo simulation. Based on the received symbol a decision is performed creating the received bit sequence. The received bit sequence is compared to the transmitted bit sequence and

the differences are accounted as errors in the transmission.

3.5.3. Outage probability

Due to the stochastic nature of the ICXT, the system can sporadically operate at a BER higher than acceptable. These high BER events that render the system inoperative can be characterized by the outage probability and are defined by the probability of the pre-FEC BER rising above a determined BER threshold [63]. In this work, a pre-FEC BER threshold of $10^{-1.8} = 1.58 \times 10^{-2}$ was considered [64]. The simulation for a given ICXT level is stopped at the hundredth occurrence of a time fraction with a higher BER than the threshold. The outage probability, P_{out}, is given by the ratio of the number of time fractions with BER higher than the threshold, $\#TF_{out}$, and the number of all the elapsed time fractions, $\#TF_{total}$, and can be written as:

$$P_{out} = \frac{\#TF_{out}}{\#TF_{total}} \tag{3.22}$$

3.6. Model verification

This section shows that all the system blocks were correctly implemented in the numerical simulator. The parameters presented in this section will be used throughout the following subsections and were used to generate the figures presented previously.

In the numerical simulator, the signal is treated as analog since no sampling is made of the photo-detected signal. Thus, the chromatic dispersion compensation is performed by using the inverse transfer function of the SMF, $1/e^{-j\overline{\beta_n}(\omega)L}$, and a large enough simulation bandwidth is used to allow for the signal's broadening such that no signal up-sampling is needed when applying the KK algorithm. For DSP implementation, the chromatic dispersion compensation can be performed using a finite impulse response filter such as [65]. Also, an upsampling factor of 3 was found to be sufficient to accommodate the spectral broadening caused by the logarithm [47]. Furthermore, the signal has the specification presented in table 3.1, the p-i-n used has unit responsivity and no frequency limitations. The electrical noise is generated in the entire simulation bandwidth, f_s, given by $f_s = R_s N_{samples}$ where $N_{samples}$ is the number of samples per symbol, and has a variance given by $\sigma_c^2 = \frac{R_\lambda^2 NEP^2}{2} f_s$ [62]. Using a NEP of 10 pW/Hz$^{1/2}$ and a simulation bandwidth of 856 GHz, which corresponds to using 2^4 samples per symbol, the electrical noise variance is $\sigma_c^2 \approx 4.28 \times 10^{-11}$W $\approx$ -73.7 dBm. In the transmitter, the bit streams are modeled as deBruijn sequences with 2^n bits and different sequences are used in the phase and quadrature components of the QAM signal. This leads to symbol sequences with different PAPR values.

The BER is estimated by both Monte Carlo simulation and EVM. The Monte Carlo simulation is performed using direct error count and stopped at the 100th error, simultaneously the EVM is calculated at each set of 2^n symbols, n varying from simulation to simulation, and averaged over all sets until 100 bit errors occur, the average EVM is then used to calculate the BER using eq. 3.21.

TABLE 3.1. Signal parameters.

Parameter	Value
Bit rate [Gbit/s]	214
Signal modulation	16-QAM
Roll-off factor	0.01
Optical signal launching power [dBm]	0
Carrier frequency [THz]	193.1

3.6.1. Fiber model

To verify if the WC-MCF is correctly implemented in the simulator we can use the amplitude of the real and imaginary components of the ICXT field at the output of the test core. The WC-MCF has 1000 RPS as in [35, 36, 59] and a skew between cores of $0.01/R_s$ [66]. Table 3.2 presents a summary of all the WC-MCF parameters. The WC-MCF has a length of 10 km, an ICXT level of -30 dB and no losses were considered in order to only characterize the ICXT evolution.

TABLE 3.2. WC-MCF parameters.

Fiber parameter	Value
Attenuation [dB/km]	0.23
Dispersion [ps/(nm km)]	17
Dispersion slope [fs/(nm² km)]	90
Reference dispersion wavelength [nm]	1550
Difference of dispersion between cores	0
Test core effective refractive index	1.4683
Interfering core effective refractive index	1.4685
Number of RPS (N)	1000
Skew [s]	$0.01/R_s \approx 1.87 \times 10^{-13}$

A continuous light source with unitary power is launched to both cores of the fiber and 10^5 samples of ICXT field are obtained at the WC-MCF output of the test core. The real, $\mathcal{R}$, and imaginary, $\mathcal{I}$, components of the ICXT field are then shown in a histogram.

Fig. 3.12 shows the histogram of the ICXT field distribution in the x polarization. The statistics of each histogram present in fig. 3.12 are presented in table 3.3. Since the theoretical probability density function has a zero mean and a variance of $N|K_{nm}|^2/2 = 5 \times 10^{-4}$, the simulated result is in good agreement with the theoretical model.

Fig. 3.13 shows the histogram of the ICXT field distribution in the y polarization. The statistics of the histograms present in fig. 3.13 are presented in table 3.4. Since the
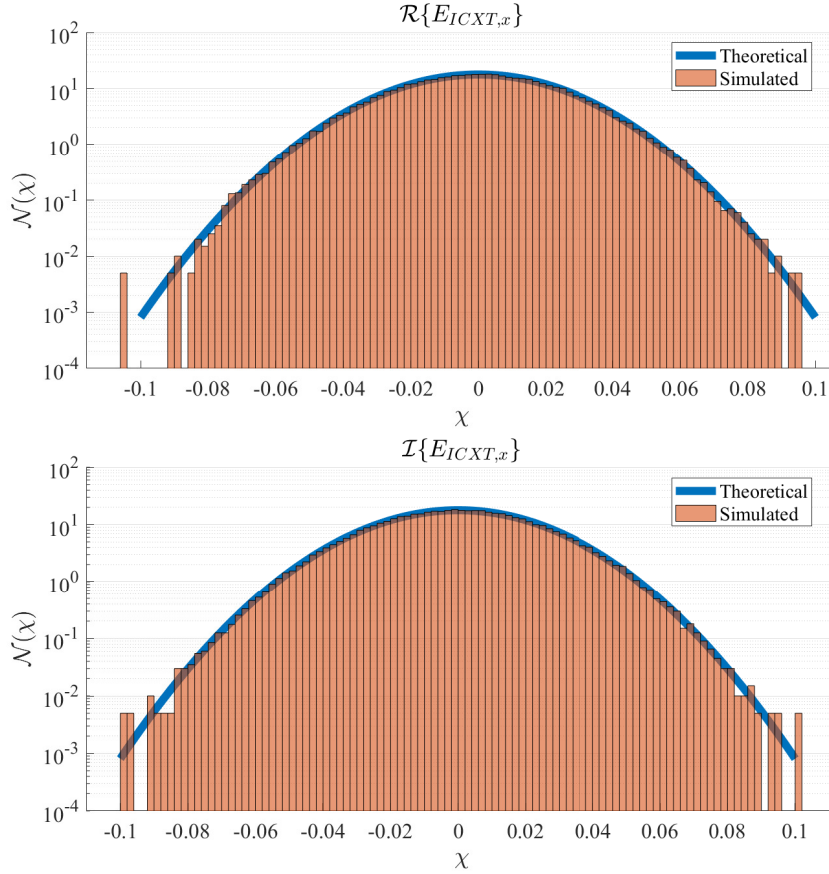
FIGURE 3.12. Histogram of the simulated distribution of the ICXT x polarization (orange bars) and theoretical profile (blue line), χ being the received signal amplitude and $\mathcal{N}(\chi)$ the probability density function.

TABLE 3.3. Mean and variance of the ICXT distributions of the x polarization.

x polarization		
$\mathcal{R}\{E_{ICXT,x}\}$	Mean	2.4917×10^{-5}
	Variance	5.0349×10^{-4}
$\mathcal{I}\{E_{ICXT,x}\}$	Mean	-3.7490×10^{-5}
	Variance	4.9864×10^{-4}

TABLE 3.4. Mean and variance of the ICXT distributions of the y polarization.

y polarization		
$\mathcal{R}\{E_{ICXT,y}\}$	Mean	7.6445×10^{-5}
	Variance	4.9809×10^{-4}
$\mathcal{I}\{E_{ICXT,y}\}$	Mean	8.0655×10^{-5}
	Variance	4.9830×10^{-4}

theoretical model has zero mean and a variance given by $N|K_{nm}|^2/2 = 5 \times 10^{-4}$ the simulation results are in good agreement with the theoretical model. Concluding that the WC-MCF was correctly implemented in the simulator.
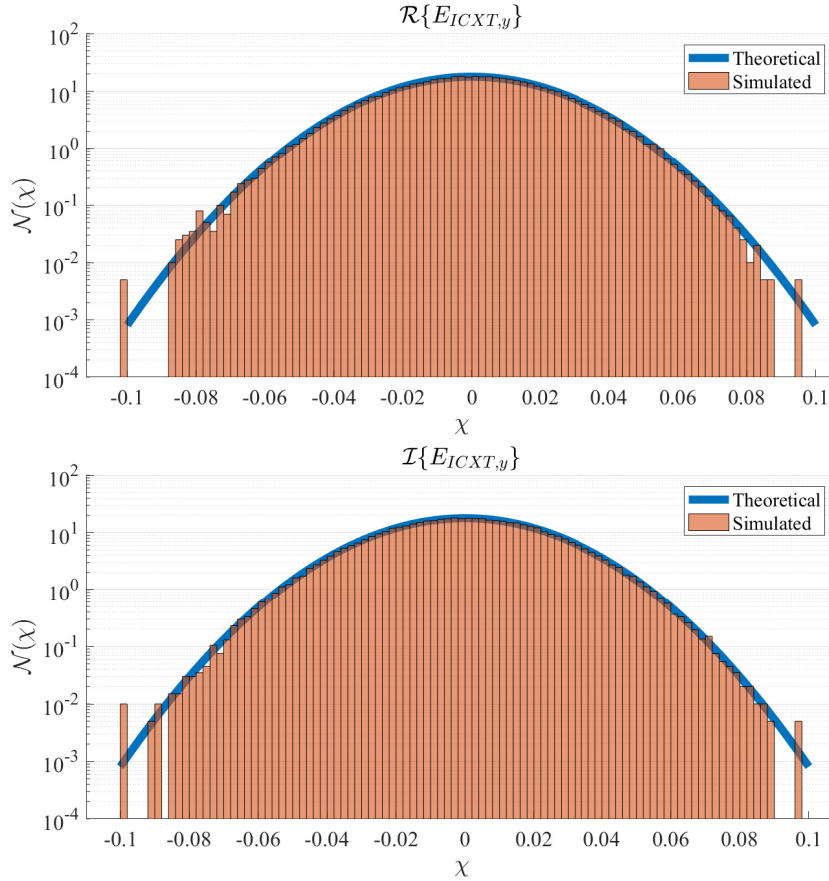
FIGURE 3.13. Histogram of the simulated distribution of the ICXT y polarization (orange bars) and theoretical profile (blue line), χ being the received amplitude and $\mathcal{N}(\chi)$ the probability density function.

3.6.2. Ideal KK algorithm

The SSB signal used with the KK algorithm has to ensure a predetermined condition, the CSPR has to be superior to the PAPR of the signal. The received symbols may not be correct if this condition is not fulfilled, increasing the BER.

Fig. 3.14 presents the constellation of the received QAM signal immediately after matched filtering when different CSPRs are considered. The signal was obtained in back-to-back operation with the signal's parameters presented in table 3.1, a PAPR of 8 dB and electrical noise were considered. The RC shaped signal was sampled at the optimum sampling time and normalized to unitary power. Fig. 3.14a shows a constellation where a CSPR of 7 dB was used. This CSPR is not superior to the PAPR and as a result the constellation is degraded, mainly in the symbols in the corners of the constellation. However, if the CSPR is superior to PAPR, as in fig. 3.14b, the constellation is very similar to the ideal constellation, although affected by electrical noise. Furthermore, the CSPR can be chosen to optimize the performance of the system.

Fig. 3.15 shows the BER as a function of the CSPR for various lengths of fiber. An SMF, with the relevant parameters present in table 3.2, was used to establish a baseline

(a) CSPR: 7 dB

(b) CSPR: 16 dB
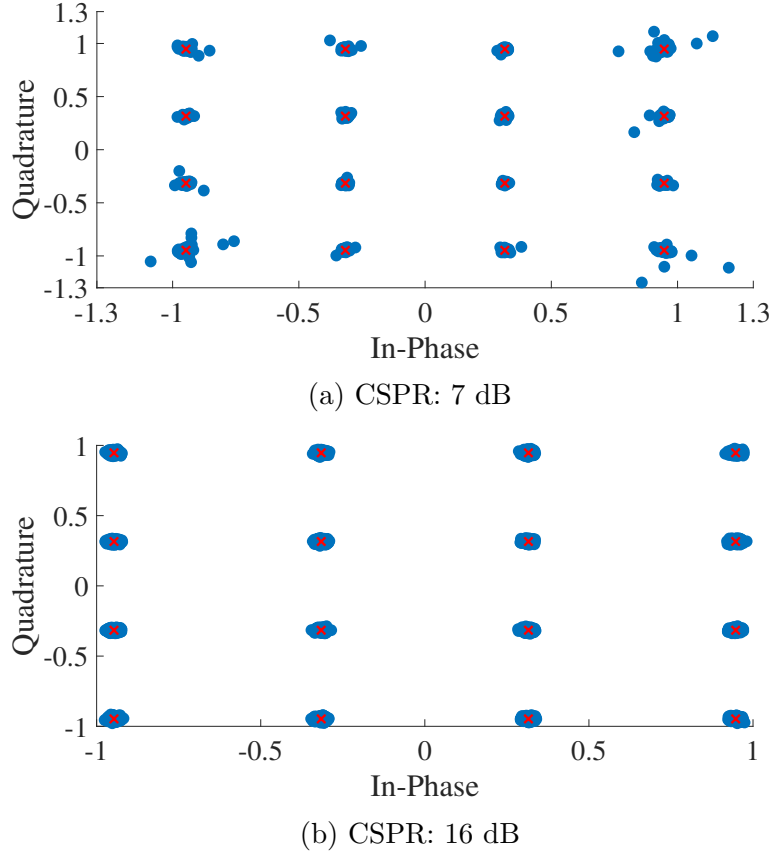
FIGURE 3.14. Normalized signal constellation affected by electric noise after ideal KK algorithm and matched filtering in back-to-back operation (blue circular markers), ideal constellation (red cross markers) with a PAPR of 8 dB and a CSPR of 7 dB in (a) and 16 dB in (b).
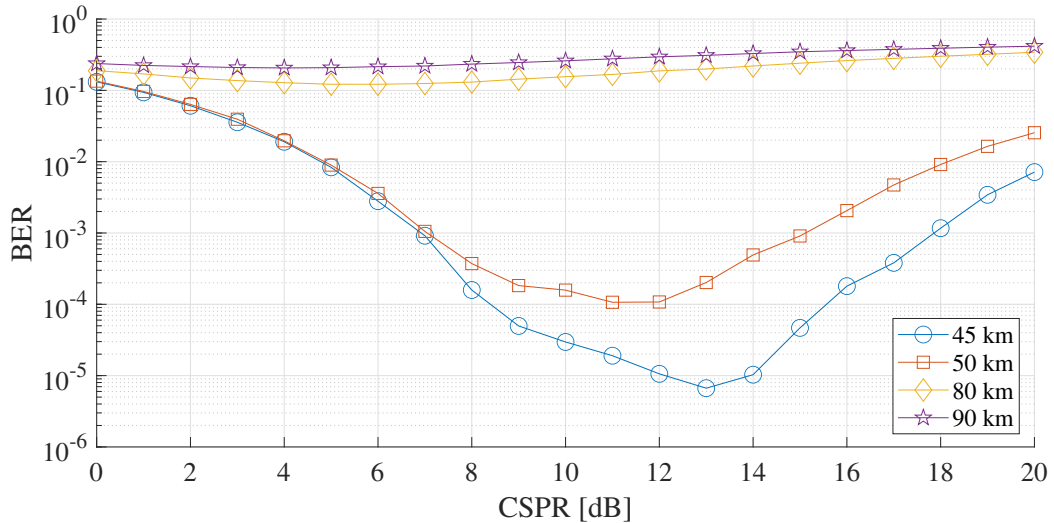
FIGURE 3.15. BER versus CSPR using an ideal KK receiver and Monte Carlo simulation for the fiber lengths of 45 km (blue circular markers), 50 km (orange square markers), 80 km (yellow diamond markers) and 90 km (violet star markers).

of the system when no ICXT is present. The signal's parameters are shown in table 3.1 and a sequence with 2^{14} symbols was used. The PAPR of the information-bearing signal is 8 dB. The BER was estimated using Monte Carlo simulation. Results of fig. 3.15 show that the optimum CSPR varies with the fiber length. This is due to the need of a strong carrier to guaranty the minimum phase condition. However, the carrier cannot be so strong that the information-bearing signal has a power comparable to the electrical noise power. If this happens, the symbols are degraded. A clear optimum CSPR can be obtain for the shorter fiber lengths; however, for the longer fiber lengths, the signal is completely degraded regardless of which CSPR is chosen.
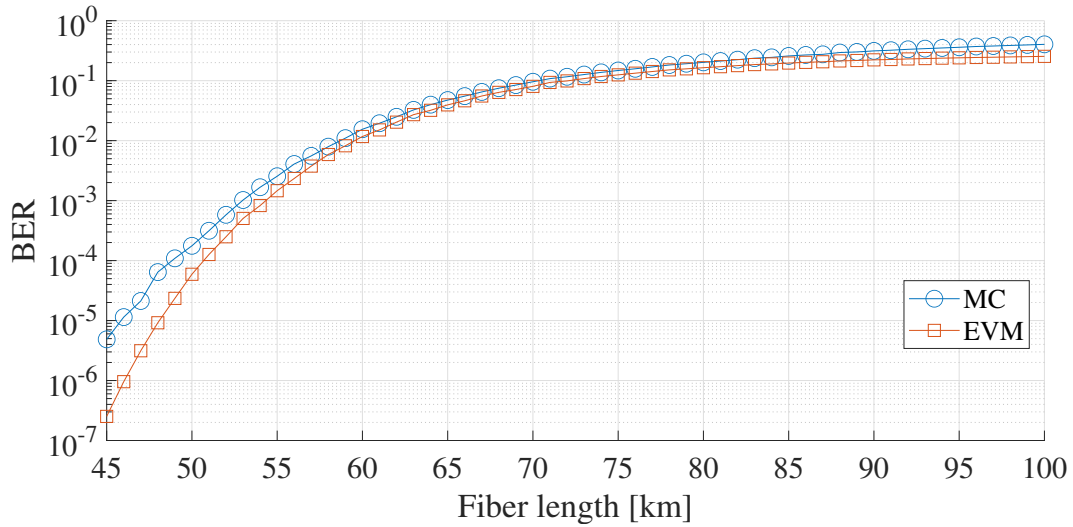
FIGURE 3.16. BER versus fiber length, calculated using Monte Carlo (blue circular markers) and EVM (orange square markers).

Fig. 3.16 shows the BER as a function of the fiber length. The BER was estimated using Monte Carlo and EVM. The signal's parameters are shown in table 3.1 and a sequence with 2^{14} symbols was used. The PAPR of the information bearing signal is 8 dB and a CSPR of 13 dB was used since it's the optimum CSPR for a 45 km fiber. It can be observed that for longer lengths of fiber the difference of BER between EVM and Monte Carlo is negligible; however, for shorter lengths of fiber a difference of approximately 3 km is present for the same BER. Using the aforementioned parameters and a fiber length of 45 km the system employing the ideal KK algorithm operates at a pre-FEC BER bellow 10^{-5}.

3.6.3. AC coupled KK algorithm

The AC coupled KK algorithm relies on the proposed metric, eq. 2.7, to assess if the introduced bias is correct.

Fig. 3.17 shows two constellation where different bias values were used. The constellations were obtained in a back-to-back configuration, the transmitted signal has a PAPR

(a) Ideal bias.

(b) Bias with an error of 0.25 of the ideal bias.
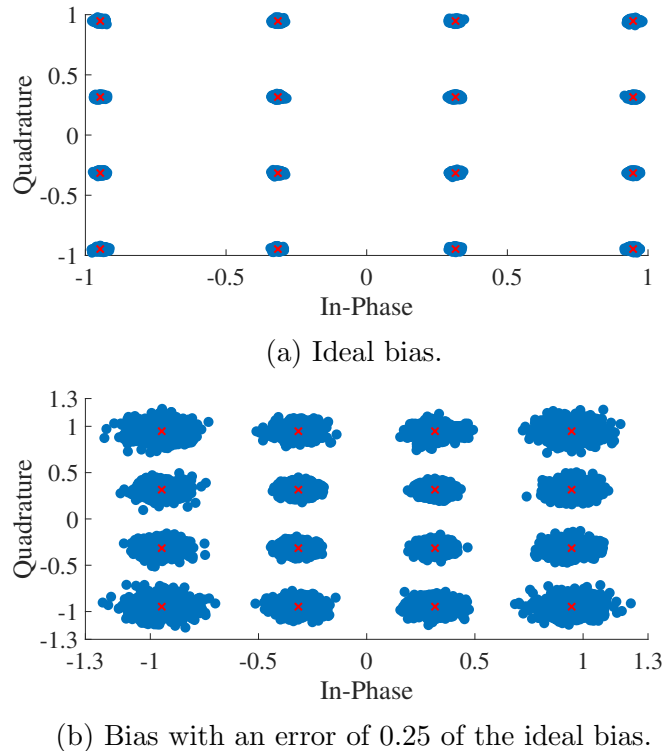
FIGURE 3.17. Normalized signal constellation affected by electric noise after AC coupled KK algorithm and matched filtering in back-to-back operation(blue circular markers), ideal constellation (red cross markers).

of 8 dB, a CSPR of 16 dB, a sequence of 2^{14} symbols, a guard band of 10% the symbol rate and the parameters presented in table 3.1 were used. The constellation presented in fig. 3.17a was obtained with the ideal bias, bias of 4.64 V with a metric of 6.03×10^{-4}, and is very similar to the ideal constellation. Fig. 3.17b shows the same signal as before but the introduced bias has an error of 25 % when compared to the ideal bias, this error significantly changes the constellation when compared to both the ideal constellation and the constellation with the ideal bias.

To compare the KK ideal algorithm and the AC coupled KK algorithm the fiber length is kept the same, 45 km, and the CSPR is optimized to this length.

Fig. 3.18 shows the BER as a function of the CSPR. The transmitted signal has the parameters presented in table 3.1 with a guard band of 10% of the symbol rate and a symbol sequence of 2^{14} symbols with a PAPR of 8 dB is used. The SMF used has the relevant parameters presented in table 3.2. The introduced bias is calculated at each 2^{14} symbols and the BER is estimated using Monte Carlo. The optimum CSPR changes with the fiber length, this is due to the reason already presented above. For a 45 km long fiber a clear minimum can be observed at a CSPR of 12 dB, 1 dB less than the optimum CSPR when using the ideal KK algorithm.

Fig. 3.19 shows the BER as a function of the fiber length. The BER was estimated using Monte Carlo and EVM. The simulation uses the same parameters as the previous one, the same bias update frequency and a CSPR of 12 dB. The discrepancy between
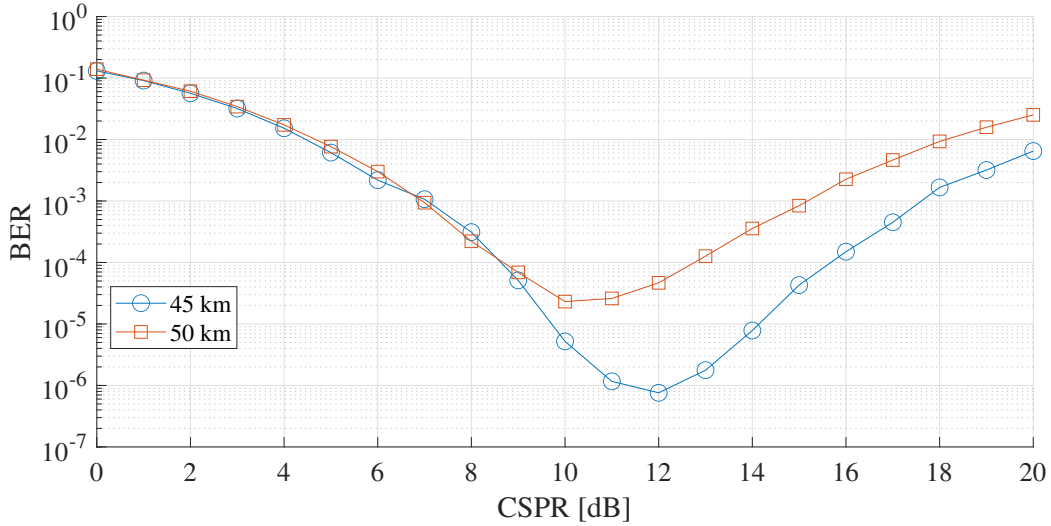
FIGURE 3.18. BER versus CSPR using an AC coupled KK receiver for a fiber length of 45 km (blue circular markers) and 50 km (orange square marker).
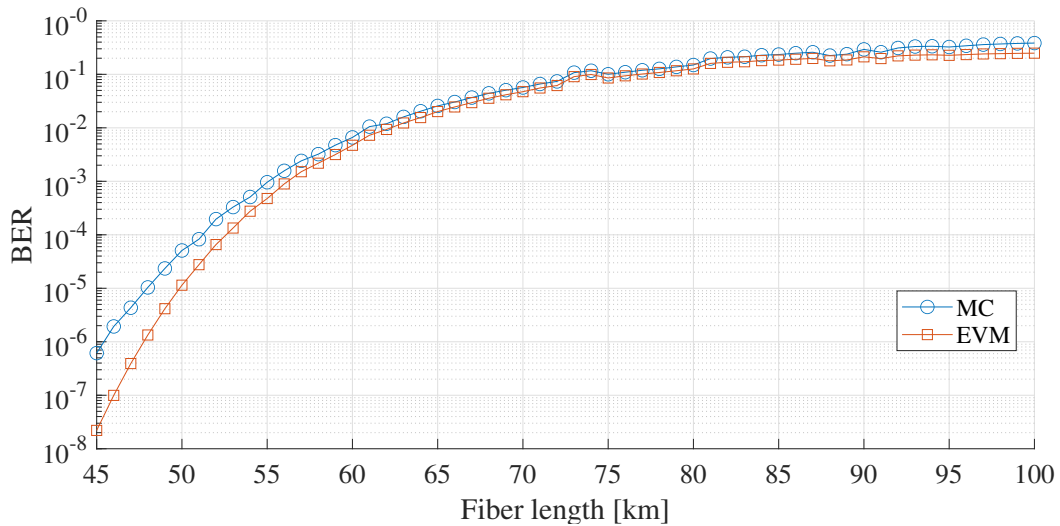
FIGURE 3.19. BER versus fiber length, estimated by Monte Carlo (blue circular markers) and EVM (orange square markers) and using an AC coupled KK receiver.

the estimation is negligible for the longer fiber lengths although, for the shorter fiber lengths an approximate 3 km difference exists between the Monte Carlo and the EVM estimation. If the system operated with the aforementioned parameters, the system's pre-FEC BER is bellow 10^{-6}, a substantial improvement, one order of magnitude, to the ideal KK algorithm. This difference is due to the bias update frequency used in the simulation, since the bias is being updated every 2^{14} symbols the CSPR is being constantly adjusted in the receiver lowering the BER of the system. If a different bias update scheme is used, the performance of the system changes. For instance, the bias can be estimated once using a small set of symbols.
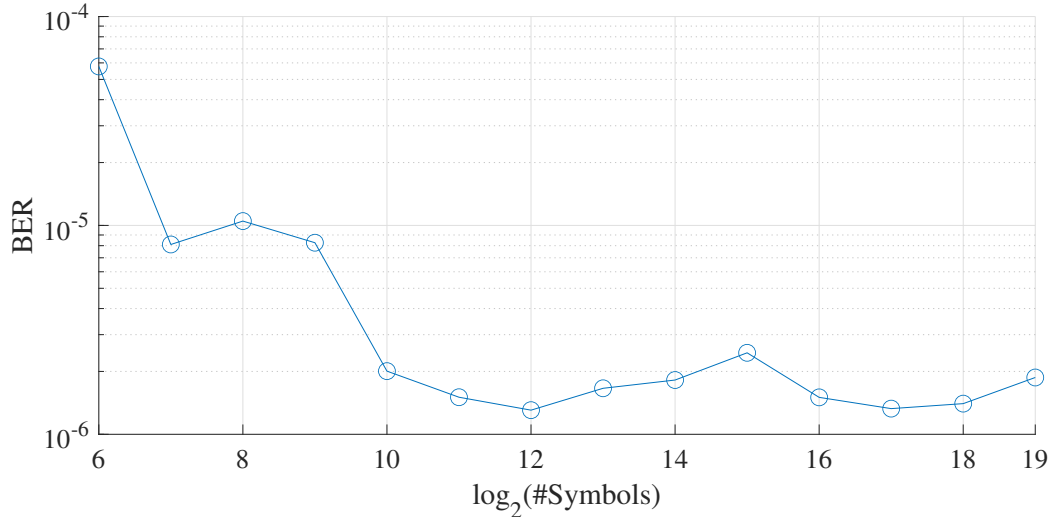
FIGURE 3.20. BER as a function of the number of symbols used to estimate the bias using an AC coupled KK algorithm and a 45 km long fiber.

Fig. 3.20 presents the BER as a function of the number of symbols used to estimate the bias introduced. A CSPR of 12 dB is used and the BER is estimated through Monte Carlo simulation using a sequence with 2^{19} symbols where just a fraction of those is used to estimate the bias. From fig. 3.20 it is possible to conclude that estimating the bias with 2^{10} symbols or more yields a BER around 2×10^{-6} while a lower number of symbols yields a worse BER. This update bias technique slightly increases the system's BER when compared to the frequent update strategy employed previously, however, this scheme decreases the connection's latency.

3.6.4. Clipping enhanced KK algorithm

Analysis the clipping enhanced KK algorithm, the the clipping level can be attained and the performance of the system in the absence of ICXT is evaluated.

Using an SMF fiber 45 km long with the relevant parameters of table 3.2. The transmitted signal used has the parameters presented in table 3.1 using sequences of 2^{19} symbols and using a CSPR of 10 dB. This sequence is chosen because has the highest PAPR of all sequences tested, 9.2 dB. Furthermore, the LPF in the correction path of the clipping enhanced KK algorithm, shown in fig. 2.9, is a rectangular filter with 60 GHz bandwidth. The optimum clipping level is calculated and shown in the following figure.

Fig. 3.21 shows the BER as a function of the normalized clipping level. The BER was estimated using Monte Carlo. The BER decreases gradually as the clipping level increases until an optimum clipping level is attained, as reported in [50]. The optimum clipping level can be found at a normalized clipping level of $10^{-0.7}$.

Fig. 3.22 shows the BER as a function of the fiber length. The fiber and transmitted signal use the aforementioned parameters and a normalized clipping level of $10^{-0.7}$. The
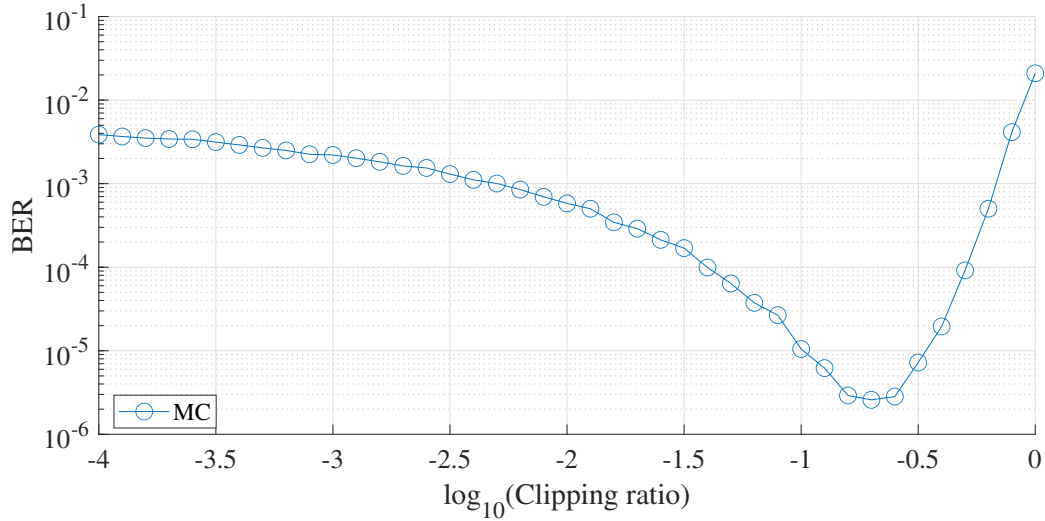
FIGURE 3.21. BER versus normalized clipping level, calculated using Monte Carlo and a 45 km long SMF with a clipping enhanced KK receiver.
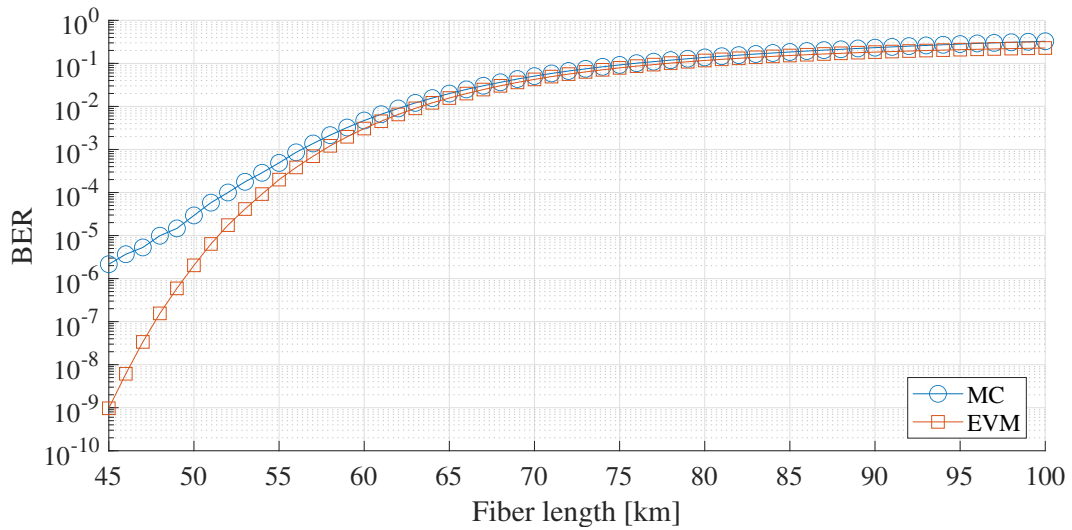
FIGURE 3.22. BER versus fiber length, estimated by Monte Carlo (blue circular markers) and EVM (orange square markers), using a clipping enhanced KK algorithm.

BER is estimated by Monte Carlo simulation and from EVM. Between the two estimation methods a discrepancy of 6 km is found for the smaller fiber lengths, however, for longer fiber lengths it is negligible. The system using the clipping enhanced KK algorithm with the aforementioned parameters operates at a pre-FEC BER bellow 3×10^{-6} for a fiber length of 45 km, an order of magnitude lower when compared to the ideal KK algorithm.

CHAPTER 4

Impact of the ICXT on the performance of the KK algorithms

This chapter presents the impact of the ICXT on the performance of the KK algorithms. A 45 km long two-core WC-MCF is employed with the MCF's parameters presented in table 3.2. Electric noise, chromatic dispersion and random polarization rotation are considered in the study. The signals launched in both cores, although uncorrelated between them, have the same characteristics, presented in table 3.1. The impact of the ICXT is analyzed in section 4.1 for the ideal KK algorithm, in section 4.2 for the AC coupled KK algorithm and in section 4.3 for the clipping enhanced KK algorithm. Finally, in section 4.4, the dependence of outage probability on the ICXT level when using different KK algorithms is evaluated and discussed.

Similarly to the previous chapter, the BER is estimated by both Monte Carlo simulation and EVM. The Monte Carlo simulation is stopped at the 100th bit error, simultaneously the EVM is calculated at each set of 2^n symbols, n varying from simulation to simulation, and averaged over all sets until 100 bit errors occur, the average EVM is then used to calculate the BER using eq. 3.21.

4.1. ICXT impact on the ideal KK algorithm

Fig. 4.1 and fig. 4.2 show a snapshot of the behavior of the system through 100 different time fractions. Each time fraction corresponds to a small time interval where the ICXT is assumed to be constant. The WC-MCF has the parameters mentioned above and an ICXT level of -20 dB is considered. In both cores, a CSPR of 13 dB and different sequences with 2^{14} symbols are used. The sequences used both have a PAPR of 8 dB.

Fig. 4.1 shows the STAXT measured in 100 different time fractions. Due to the stochastic properties of the ICXT induced in the test core, the STAXT varies randomly over time with differences of 15 dB from time fraction to time fraction with a maximum STAXT close to -25 dBm and a minimum close to -40 dBm. This type of variation poses a serious challenge for ICXT mitigation, since the increased ICXT raises the number of bit errors in the test core.

Fig. 4.2 shows the BER through 100 different time fractions. The BER is calculated using Monte Carlo simulation and using the EVM evaluated at each set of 2^{14} symbols. From fig. 4.2 it can be seen that some time fractions have a BER significantly superior when compared with the absence of ICXT. This effect is so pronounced that some time
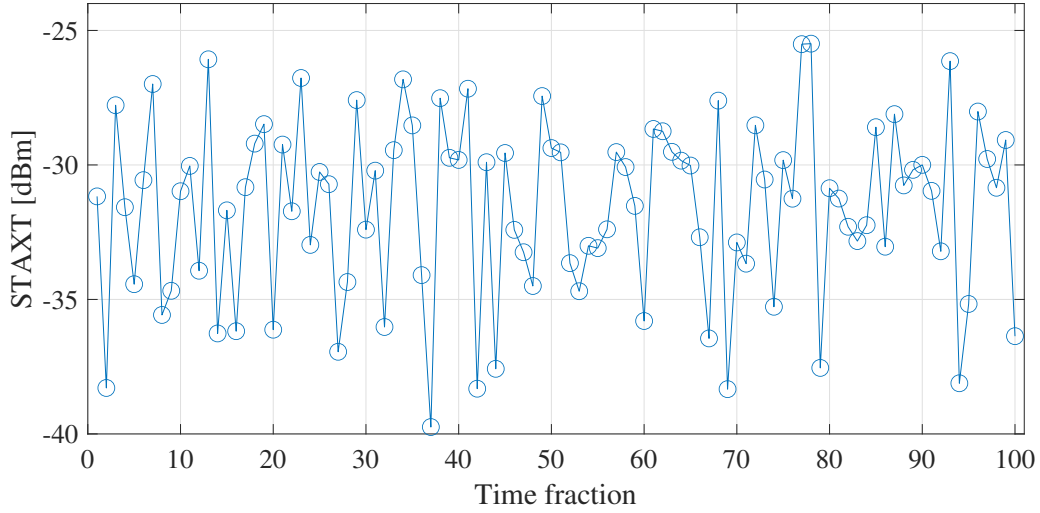
FIGURE 4.1. STAXT versus time fraction, using a 45 km long WC-MCF with an ICXT level of -20 dB.
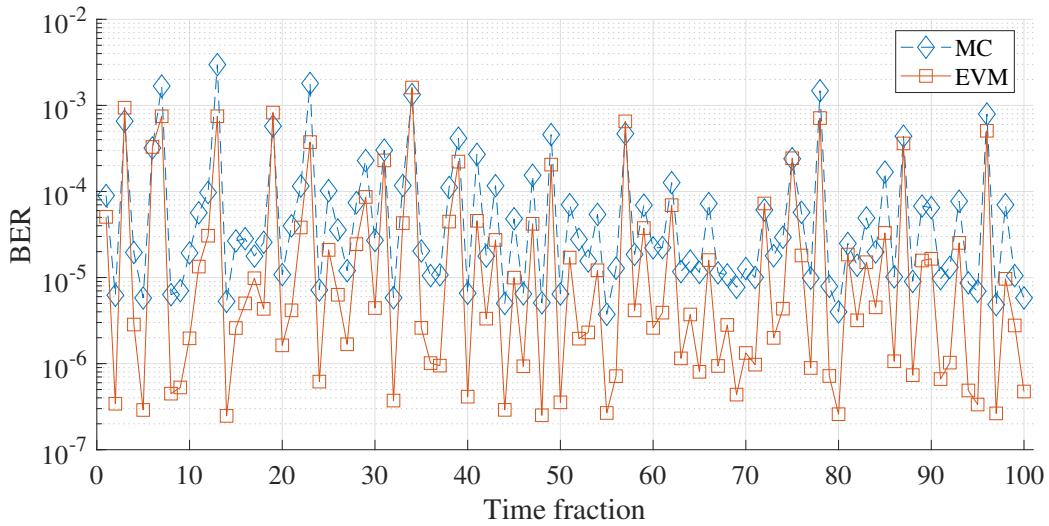
FIGURE 4.2. BER as a function of the time fraction, calculated using Monte Carlo (blue diamond markers) and EVM (orange square markers), for a 45 km long WC-MCF and an ICXT level of -20 dB.

fractions have a BER superior to 10^{-3}, where the BER in the absence of ICXT is bellow 10^{-5}. The time fractions that have a higher BER are clearly identified by Monte Carlo and EVM. The same cannot be said for the lower BER time fractions where a significant difference is present between both estimation methods. The BER evaluated through the EVM assumes that the signal is affected by Gaussian noise, an invalid assumption for these time fractions. In low skew WC-MCF, $|S_{mn} \times R_s| \ll 1$, the ICXT induced in the test core depends of the symbol present in the interfering core at the same symbol period and of the STAXT present in that time fraction [64]. If a time fraction has a high STAXT, the variation of the symbols in the test core increases leading to a worse BER in that time fraction.

Moreover, if the BER of a time fraction is higher than the FEC threshold, 4.5×10^{-3}, the FEC cannot compensate the errors present in the time fraction and, after decoding, the system will operate with an intolerable amount of errors, at which point the service cannot be maintained and an outage event occurs. These events that render the system inoperable must have a low probability of happening such that the system's availability is guarantied.

The simulator uses different symbol sequences with different sizes to model the bit streams in the transmitter. As a result, there is a need to demonstrate that the simulator is agnostic to the symbol sequence that is being used.
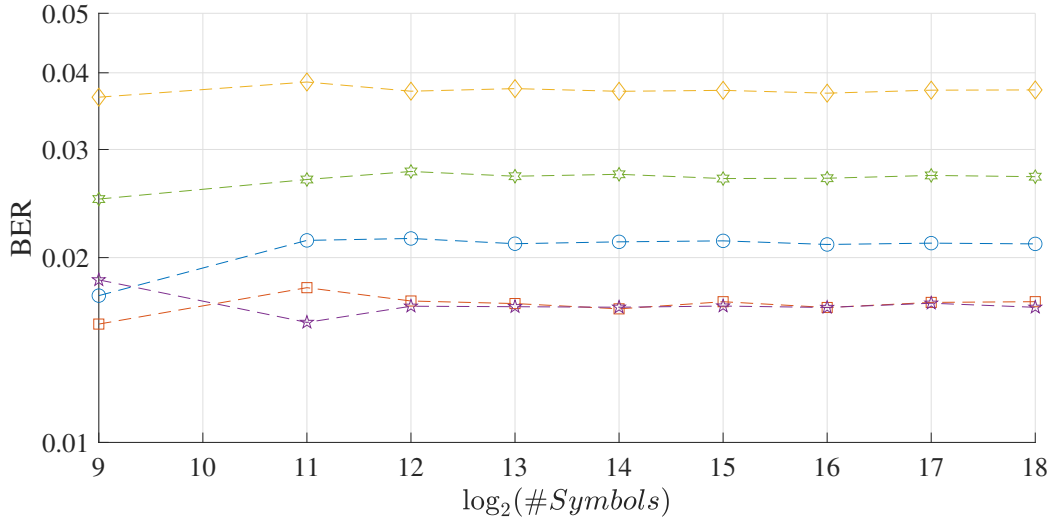
FIGURE 4.3. BER versus $\log_2(\#Symbols)$ using ideal KK receiver and a 45 km long WC-MCF with an ICXT level of -10 dB. Different marker/color combinations represent different time fractions.

Fig. 4.3 shows the BER as a function of the number of symbols of the bit stream. The signal launched in each core has the parameters presented in table 3.1 and a CSPR of 13 dB. The BER is evaluated using the EVM considering only 2^n symbols where n takes the values in the x axis, while maintaining the ICXT field set to -10 dB and the same random phase shifts when changing the sequence size. Different marker/color combinations represent different time fractions. Each color/marker line shows the BER where the transmitted sequences have different sizes, but the RPS are kept the same and inserted in the same locations. From the analysis of fig. 4.3, a similar behavior is found for the various sequences tested. Furthermore, to correctly estimate the outage probability, the BER of a time fraction has to be correctly estimated in the neighborhood of the considered threshold for a outage event, $10^{-1.8} = 1.58 \times 10^{-2}$. Thus, the size of the symbol sequence can be adequately chosen to correctly evaluate the system performance using the smallest number of symbols, reducing simulation time. From fig. 4.3, it is seen that using a sequence with 2^{12} symbols already presents minimal variations when compared to the sequences with a higher number of symbols. Therefore, to estimate the outage

probability in section 4.4, the system using the ideal KK algorithm uses a sequence with 2^{13} symbols, guarantying a good accuracy of the outage probability estimation.

4.2. ICXT impact on the AC coupled KK algorithm

The analysis performed for the ideal KK algorithm can be made for the AC coupled KK algorithm. The signals launched into the test core and the interfering core have the same parameters, shown in table 3.1, an CSPR of 12 dB and a guard band of 10% of the symbol rate between the optical carrier and the information bearing signal.
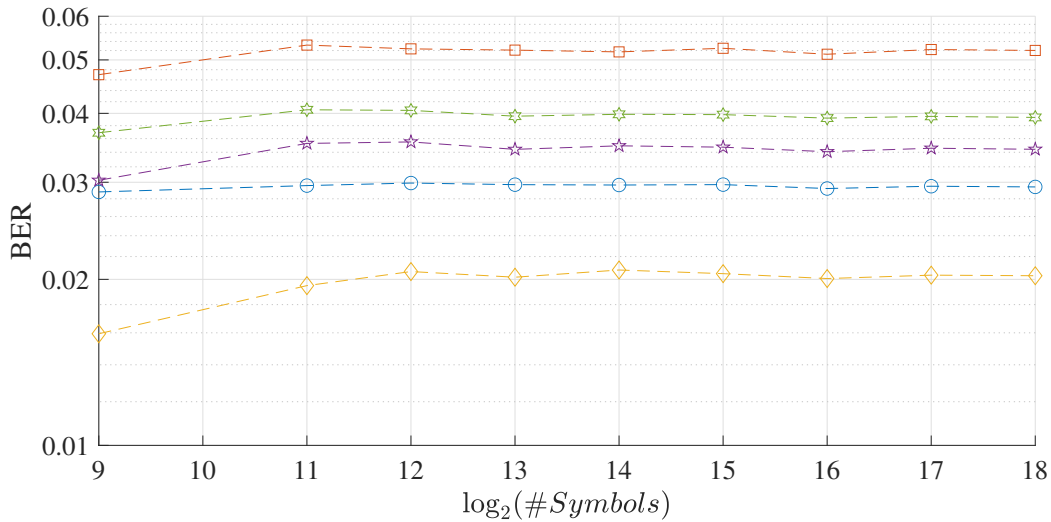
FIGURE 4.4. BER versus $\log_2(\#Symbols)$ using an AC coupled KK algorithm and a WC-MCF 45 km long with an ICXT level of -10 dB. Different marker/color combinations represent different time fractions.

Fig. 4.4 shows the BER as a function of the symbols of the bit stream under the same conditions as in fig. 4.3 with the bias being optimized for each set of 2^n symbols where n takes the values of the x axis. From fig. 4.4, the behavior of the system when different sequence sizes are used is shown, verifying that the system is agnostic to the size of the bit stream. Moreover, the size of the symbol sequence can be adequately selected so that in the neighborhood of the threshold for an outage event the BER is correctly evaluated using the minimum number of symbols. A sequence with just 2^{12} symbols already presents minimal variation in the BER estimation when compared to sequences with bigger size sequences. Sequences of 2^{13} symbols are used for the simulation of the outage probability in section 4.4.

The behavior of the system through several time fractions is captured in fig. 4.5 and fig. 4.6.

Fig. 4.5 shows the BER variation through 100 different time fractions. The signal and the WC-MCF have the already mentioned parameters with an ICXT level of -20 dB and sequences of 2^{14} symbols with a bias update at each set of 2^{14} symbols. The BER is
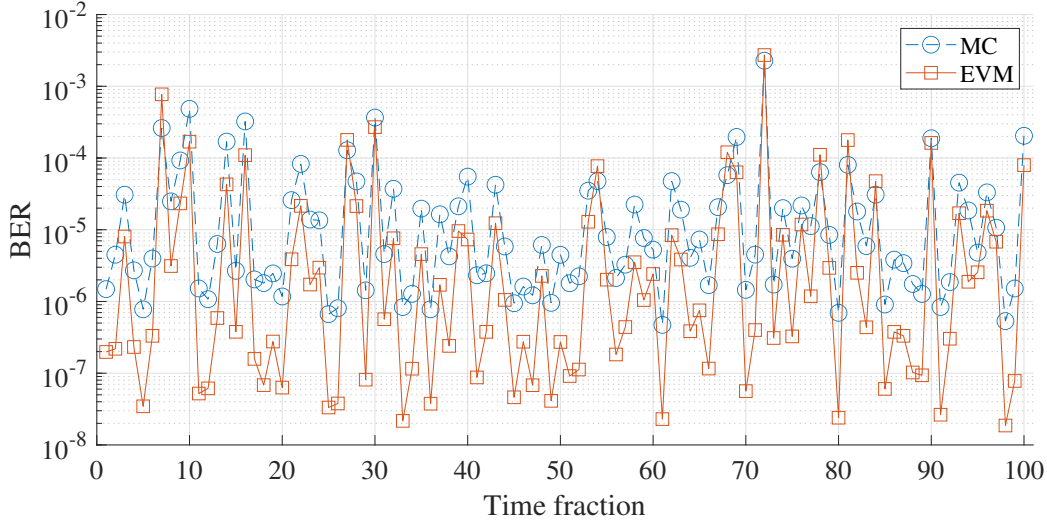
FIGURE 4.5. BER as a function of the time fraction, calculated using Monte Carlo (blue circular markers) and EVM (orange square markers), using an AC coupled KK algorithm and a 45 km long WC-MCF and an ICXT level of -20 dB.

estimated both using Monte Carlo simulation and from the EVM evaluated at each set of 2^{14} symbols. From fig. 4.5, it is seen that the high BER time fractions are correctly estimated by both estimation methods, Monte Carlo and EVM, in contrast to the low BER time fractions where a significant discrepancy is found between both estimation methods. This can be attributed to the fact that the assumptions made in the derivation of eq. 3.21 are not met in this particular case. Furthermore, the random nature of the ICXT degradation is clearly shown in two adjacent time fractions, #71 and #72. Time fraction #71 has a BER estimated by both EVM and Monte Carlo of BER $= 2 \times 10^{-3}$. However, the next time fraction, #72, has a BER estimated using the EVM of BER $= 3 \times 10^{-7}$ and using Monte Carlo of BER $= 2 \times 10^{-6}$, which represents a difference of one order of magnitude between estimation methods and several orders of magnitude when compared to the previous time fraction.

Fig. 4.6 shows the STAXT as a function of the time fraction. The STAXT is calculated in each time fraction shown in fig. 4.5. The STAXT varies randomly from time fraction to time fraction with differences of 15 dB between time fractions, a maximum around -25 dBm and minimum around -40 dBm. As previously explained, in this low skew situation, if a time fraction has a high STAXT the symbols present in the interfering core make the corresponding symbols (of the same symbol period) of the test core vary. This can lead to an increased BER. In contrast, in low STAXT time fractions the variation induced in the test core is minimal, leading to a BER similar to the one in the absence of ICXT.

Using a different bias update strategy can change the performance of the system in the absence of ICXT, and the same analysis can be performed when ICXT is present.
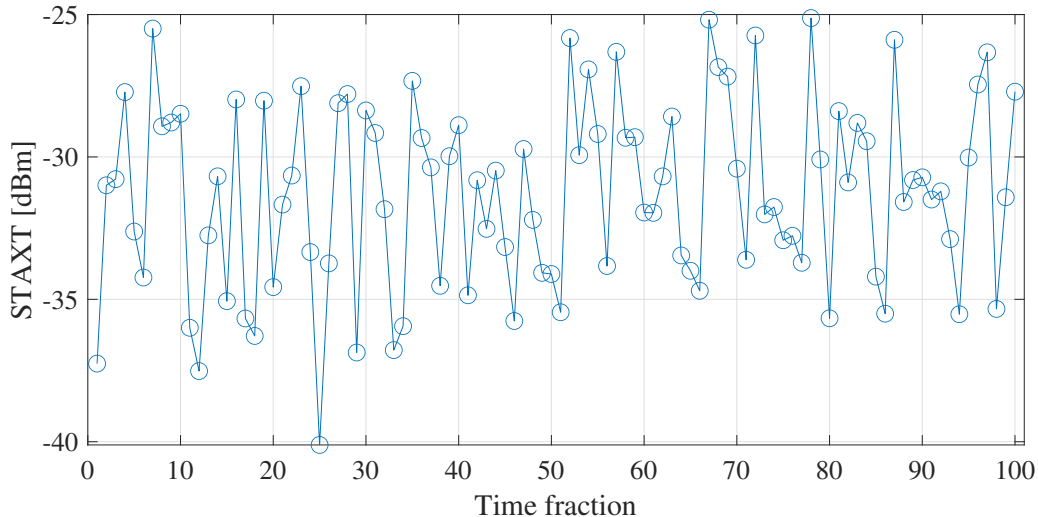
FIGURE 4.6. STAXT as a function of the time fraction, using an AC coupled KK algorithm and a 45 km long WC-MCF and an ICXT level of -20 dB.

Fig. 4.7 shows the BER as a function of the number of symbols used to estimate the bias. The BER is estimated through Monte Carlo simulation using a sequence of 2^{19} symbols with the bias being estimated once in a sub-set of those symbols. The WC-MCF and the transmitted signal have the aforementioned parameters. Fig. 4.7a, where a -20 dB ICXT level is used, shows several time fractions with a low BER. It is possible to see that using 2^{10} symbols to estimate the bias provides a BER with minimal variations in all the presented time fractions, which is similar to the case in the absence of ICXT. In contrast, in fig. 4.7b, where a -10 dB ICXT level is used, the ICXT severely degrades the signal and the impact of the number of symbols used to estimate the bias is reduced when compared to the absence of ICXT and to the previous case.

4.3. ICXT impact on the clipping enhanced KK algorithm

Fig. 4.8 and fig. 4.9 show a snapshot of the behaviour of the system in the presence of ICXT. The WC-MCF has the parameters mentioned above and an ICXT level of -20 dB. In both cores a CSPR of 10 dB is used. Uncorrelated sequences with 2^{11} symbols are used in each core. Since different sequences are used in each core, the PAPR of the sequence used in the test core is 8 dB and 7 dB in the interfering core.

Fig. 4.8 shows the BER as a function of the time fraction. The BER is calculated using Monte Carlo simulation and from the EVM evaluated at each set of 2^{11} symbols. The estimation of the low BER time fractions have a discrepancy of several orders of magnitude between estimation methods, however, the high BER time fractions are well identified using both estimation methods. This can be attributed to the fact that the assumptions made in eq. 3.21 are valid in one case and not in the other. The high BER
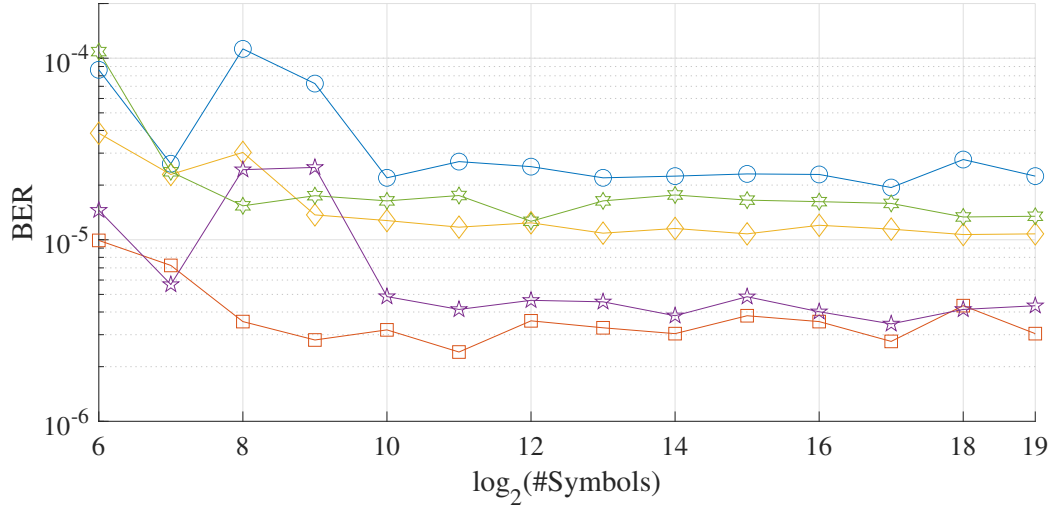
(a) ICXT level: -20 dB
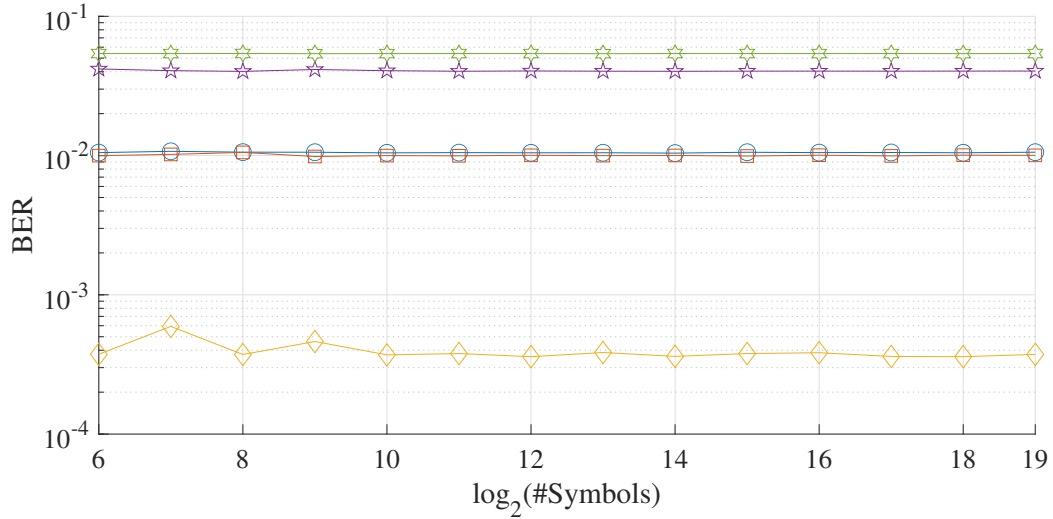
(b) ICXT level: -10 dB

FIGURE 4.7. BER as a function of the number of symbols used to estimate the bias in two different ICXT level situations (different markers represent different time fractions) using 45 km long WC-MCF and an AC coupled KK algorithm.

time fractions, such as time fractions #7 and #14, have a BER several orders of magnitude superior to the system's BER in the absence of ICXT.

Fig. 4.9 shows the STAXT introduced by the WC-MCF of the previous figure as a function of the time fraction. The STAXT swings from -25 dBm to -41 dBm, a 16 dB difference between time fractions. Furthermore, in the time fractions where the STAXT is close to -25 dBm, such as time fraction #7 and #14, the BER is increased by several orders of magnitude. The BER increases in the high STAXT time fractions have the same justification already presented in the previous sections.
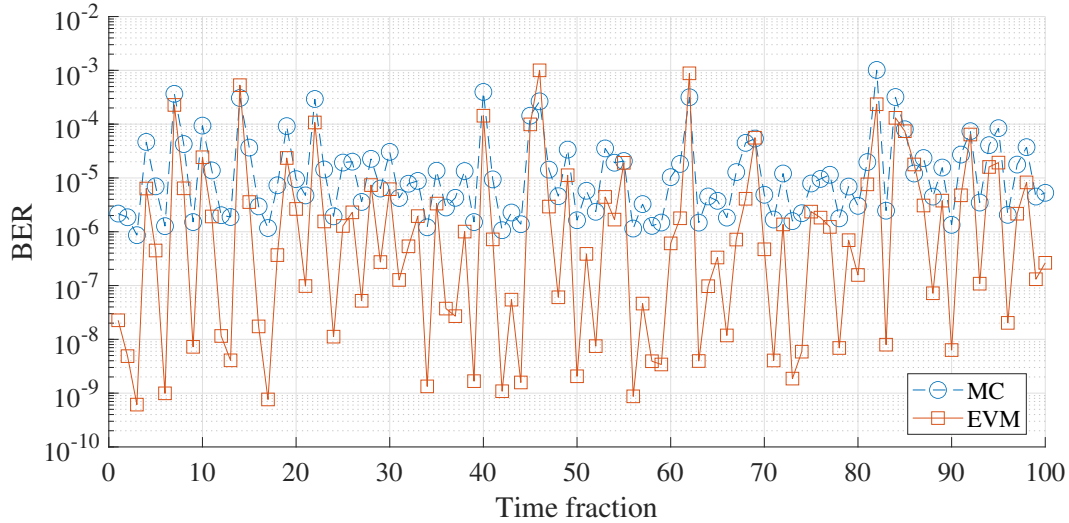
FIGURE 4.8. BER as a function of the time fraction using a clipping enhanced KK algorithm and a 45 km long WC-MCF with an ICXT level of -20 dB with the BER estimated by Monte Carlo (blue circular markers) and EVM (orange square markers).
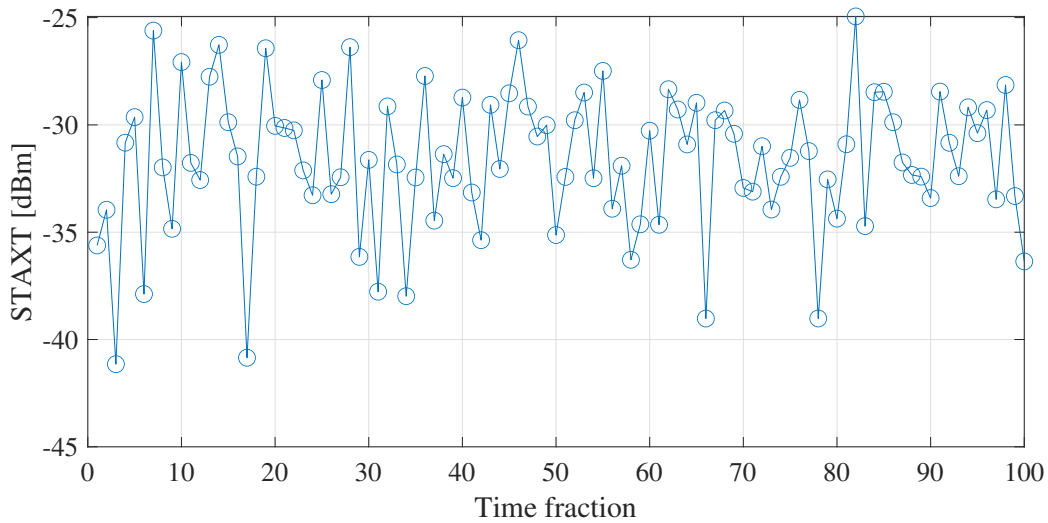
FIGURE 4.9. STAXT as a function of the time fraction using a clipping enhanced KK algorithm and a 45 km long WC-MCF with an ICXT level of -20 dB.

To assess that the simulation is not dependent of the symbol sequence used, several sequences with different sizes are tested. For all the sequences tested the highest PAPR is of 9.2 dB meaning that the minimum phase condition is always fulfilled.

Fig. 4.10 shows the BER as a function of the transmitted symbol sequence size. The transmitted signal and the WC-MCF have the aforementioned parameters and the WC-MCF has an ICXT level of -10 dB. The BER is estimated using the EVM based on a single set of 2^n symbols with n taking the values of the x axis. Different marker/color combinations represent different time fractions. Each color/marker line shows the BER
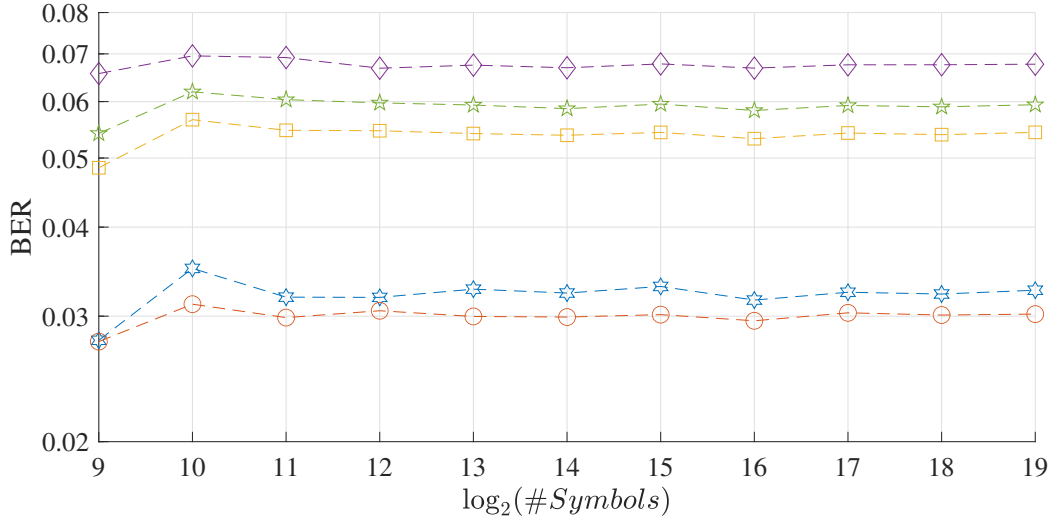
FIGURE 4.10. BER versus $\log_2(\#Symbols)$ using clipping enhanced KK receiver, an ICXT level of -10 dB and a 45 km long MCF. Different marker/color combinations represent different time fractions.

where the transmitted sequences have different sizes, but the RPS are kept the same and inserted in the same locations. A similar behavior is found for all the sequences tested proving that the system is agnostic to the sequence size. Furthermore, the symbol sequence size can be adequately chosen such that in the neighborhood of the BER threshold for an outage event the BER is correctly evaluated using the minimum number of symbols. From fig. 4.10, it is possible to see that the BER estimated using sequences with 2^{11} symbols or higher presents small variations, making this size the minimal that can be used to adequately estimate the BER. Sequences with 2^{11} symbols were used for the outage probability simulation.

4.4. Outage probability

Since the outage probability introduced by the ICXT has to be kept low enough, it is a crucial information in the design of the MCFs to be used in DCs. This directly impacts the physical characteristics of the fiber, such as core-to-core distance which in turn limits the number of cores possible in the MCFs. This dictates the achievable gains of using MCF technology in DCs.

Fig. 4.11 presents the outage probability of the system as a function of the ICXT level when employing the ideal KK algorithm, the AC coupled KK algorithm and the clipping enhanced KK algorithm. The aforementioned two core WC-MCF was used. The signal parameters are presented in table 3.1. When using the AC coupled receiver a guard band of 10% of the symbol rate is introduced between the information-bearing signal and the optical carrier. The ideal KK algorithm used an optimized CSPR for 45 km, 13 dB, and a sequence with 2^{13} symbols. Similarly, the AC coupled KK algorithm also used a symbol
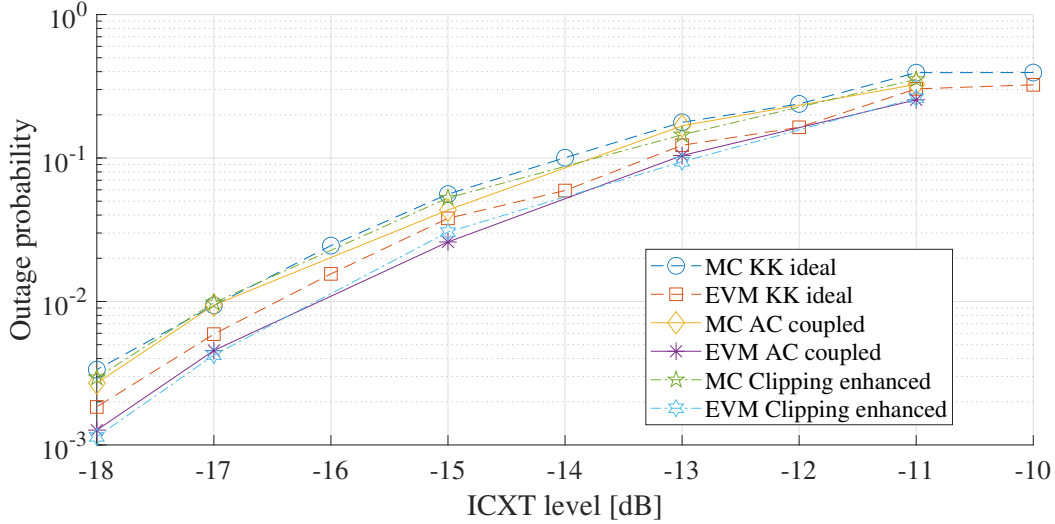
FIGURE 4.11. Outage probability as a function of the ICXT level, using an ideal KK algorithm: Monte Carlo (blue circular markers, dashed line), EVM (orange square markers, dashed line); using an AC coupled KK algorithm: Monte Carlo (yellow diamond markers, solid line), EVM (violet star markers, solid line) and using clipping enhanced KK algorithm: Monte Carlo (green pentagram markers, dash-dotted line), EVM (cyan hexagram markers, dash-dotted line).

sequence with 2^{13} symbols but a CSPR of 12 dB since these are the optimum values for this receiver and distance. The introduced bias is calculated at each set of 2^{13} symbols representing the best possible case for this receiver. Finally, the clipping enhanced KK algorithm used sequences with 2^{11} symbols with a CSPR of 10 dB. Different WC-MCF realizations (with independent RPS) are considered in each time fraction, consisting of 2^{n} symbols. For each ICXT level, the outage probability simulation is stopped when 100 time fractions with a BER superior to the outage threshold are accounted for. As expected, the outage probability decreases when the ICXT level gets lower. In all algorithms, the outage probability estimated using Monte Carlo is overestimated to the one using the EVM, with a discrepancy smaller than 1 dB. Finally, the AC coupled KK algorithm and the clipping enhanced KK algorithm present a lower outage probability than the ideal KK algorithm.

In the case of the AC coupled KK algorithm, its better performance can be attributed to the bias update frequency used. With the constant bias update, it is ensured that the system is always working where the metric is at a minimum point. This constantly adjusts the CSPR of the received signal, reducing the number of times that the signal encircles the origin, performing at its best. In the case of the clipping enhanced KK algorithm, the negative excursions of the logarithm as the signal approaches zero are limited. These excursion would produce large fast modulations at the output of the Hilbert transform which would cause errors. In the absence of all effects that degrade the received signal, these excursions do not occur and the system does not introduce errors. However, in the

presence of noise, chromatic dispersion and ICXT these excursions can happen. If they are limited by clipping then a better performance is obtained when compared to the ideal KK algorithm.

All algorithms present a high outage probability, close or superior to 10^{-1}, for ICXT levels of -13 dB or higher. Due to the simulation time required, lower outage probabilities were not possible to obtain. For instance, using an i7-4790K processor with 32 GB of RAM, the simulation for an ICXT level of -18 dB took 25 days, all the points for the ideal KK algorithm took two months and for the AC coupled KK algorithm a month and a half. For the clipping enhanced KK algorithm the simulation time was greatly reduced as a result of using a smaller symbol sequence, however, the estimation accuracy is inferior. For an ICXT level of -18 dB, a maximum outage probability of 4×10^{-3} and a minimum of 10^{-3} was achieved. Lastly, based on the results presented above it is reasonable to conclude that the EVM can be used to estimate the outage probability of a system leading to an error on the ICXT level estimation not exceeding 0.8 dB for an outage probability of 10^{-3}.

CHAPTER 5

Conclusion

Here the main conclusions of this work and some proposals for future work are presented.

5.1. Final conclusion

In this work, the ICXT impact on short-reach networks using different KK algorithms was analysed. In this study, un-amplified links with electrical noise, chromatic dispersion and random polarization rotation were considered. Furthermore, the best possible case was considered since all the receivers were analogue. If the receivers were implemented digitally a power penalty would be expected.

Chapter 2 presents a review of the main impairments in DCs and introduces the technologies used in this work to increase the capacity in DC links. One of the proposed ways to increase capacity is the use of WC-MCF as transmission fiber with the other being the use of KK receivers to increase spectral efficiency at a low cost. Several variations of the KK algorithm are analysed with different strengths and weaknesses.

Chapter 3 presents the system model and an in-depth description of the blocks that comprise the system. The differences between the systems are presented since different KK algorithms require different SSB signals to function properly. Furthermore, a baseline of the system performance in the absence of ICXT is established to evaluate how the ICXT induced by the WC-MCF affects the system.

Chapter 4 presents a snapshot of the behaviour of the WC-MCF for all the KK algorithms considered. The ICXT makes the BER vary from time fraction to time fraction with some time fractions having a BER higher than acceptable. Finally, as some time fractions have a BER higher than tolerable, the outage probability is calculated for all the different KK algorithms using Monte Carlo simulation and EVM.

From section 4.4, it is possible to conclude that estimating the system's outage probability from EVM has an error not exceeding 0.8 dB for an outage probability of 10^{-3}. Moreover, the ideal KK algorithm has the worst performance of all the tested KK algorithms while the AC Coupled KK algorithm presents a lower outage probability at the expense of much higher receiver complexity and latency. In contrast, the clipping enhanced KK algorithm has a comparable performance to the AC coupled KK algorithm and it is better than the ideal KK algorithm, it also uses a lower CSPR, and a much simpler scheme when compared to the AC coupled KK algorithm. The ideal KK algorithm

performs worse because it fails to reduce the events where the signal plus carrier plus noise plus ICXT combination approaches the origin. Since the AC coupled KK algorithm, with the frequent bias update, and the clipping enhanced KK algorithm reduce these events, they perform better.

5.2. Future work

From the analysis presented in the previous chapters some suggestions for future work can be made, such as:

- Evaluate the system's performance in optical amplified links.
- Consider digitization of the photo-current and evaluate its impact on the system performance.
- Study the noise distribution at the output of the KK algorithm, enabling analytical analysis of the system's performance.

Bibliography

[1] "Cisco annual internet report, 2018 - 2023," 2 2018.

[2] H. Waldman, "The impending optical network capacity crunch," in *2018 SBFoton International Optics and Photonics Conference (SBFoton IOPC)*, pp. 1–4, 2018.

[3] R. Urata, H. Liu, X. Zhou, and A. Vahdat, "Datacenter interconnect and networking: From evolution to holistic revolution," in *2017 Optical Fiber Communications Conference and Exhibition (OFC)*, pp. 1–3, 2017.

[4] J. Krause Perin, A. Shastri, and J. M. Kahn, "Datacenter links beyond 100gbit/s per wavelength," *Optical Fiber Technology*, vol. 44, pp. 69 – 85, 2018. Special Issue on Data Center Communications.

[5] S. Kumar, G. Papen, K. Schmidtke, and C. Xie, "Chapter 14 - intra-data center interconnects, networking, and architectures," in *Optical Fiber Telecommunications VII* (A. E. Willner, ed.), pp. 627 – 672, Academic Press, 2020.

[6] J. Wei, T. Rahman, S. Calabrò, N. Stojanovic, S. B. Hossain, C. Xie, M. Kuschnerov, and Z. Ye, "Transmission of 250 gb/s net rate per lambda using imdd pam-6 and pam-8," in *2020 Opto-Electronics and Communications Conference (OECC)*, pp. 1–3, 2020.

[7] D. Zou, F. Li, Z. Li, W. Wang, Q. Sui, Z. Cao, and Z. Li, "100g pam-6 and pam-8 signal transmission enabled by pre-chirping for 10-km intra-dci utilizing mzm in c-band," *Journal of Lightwave Technology*, vol. 38, pp. 3445–3453, 7 2020.

[8] R. Kamran, S. Naaz, S. Goyal, and S. Gupta, "High-capacity coherent dcis using pol-muxed carrier and lo-less receiver," *Journal of Lightwave Technology*, vol. 38, pp. 3461–3468, 7 2020.

[9] R. S. Kerdock and D. H. Wolaver, "Atlanta fiber system experiment: results of the atlanta experiment," *The Bell System Technical Journal*, vol. 57, no. 6, pp. 1857–1879, 1978.

[10] "G.652 : characteristics of a single-mode optical fibre and cable," 11 2016.

[11] G. P. Agrawal, *Fiber-Optic Communication Systems*. Wiley, 4 ed., 10 2010.

[12] P. J. Winzer, D. T. Neilson, and A. R. Chraplyvy, "Fiber-optic transmission and networking: the previous 20 and the next 20 years [invited]," *Opt. Express*, vol. 26, pp. 24190–24239, Sep 2018.

[13] "G.655 : characteristics of a non-zero dispersion-shifted single-mode optical fibre and cable," 11 2009.

[14] A. M. Vengsarkar, A. E. Miller, and W. A. Reed, "Highly efficient single-mode fiber for broadband dispersion compensation," in *Conference on Optical Fiber Communication/International Conference on Integrated Optics and Optical Fiber Communication*, p. PD13, Optical Society of America, 1993.

[15] A. M. Vengsarkar, A. E. Miller, M. Haner, A. H. Gnauck, W. A. Reed, and K. L. Walker, "Fundamental-mode dispersion-compensating fibers: design considerations and experiments," in *Conference on Optical Fiber Communication*, p. ThK2, Optical Society of America, 1994.

[16] A. C. Hart, R. G. Huff, and K. L. Walker, "Method of making a fiber having low polarization mode dispersion due to a permanent spin," Mar 1994. U.S. Patent 5298047.

[17] P. P. Mitra and J. B. Stark, "Nonlinear limits to the information capacity of optical fibre communications," *Nature*, vol. 411, pp. 1027–1030, 2001.

[18] R. Dar, M. Shtaif, and M. Feder, "New bounds on the capacity of the nonlinear fiber-optic channel," *Opt. Lett.*, vol. 39, pp. 398–401, Jan 2014.

[19] R. J. Essiambre, G. J. Foschini, G. Kramer, and P. J. Winzer, "Capacity limits of information transport in fiber-optic networks," *Physical Review Letters*, vol. 101, p. 163901, 10 2008.

[20] R. J. Essiambre, G. J. Foschini, P. J. Winzer, G. Kramer, and B. Goebel, "Capacity Limits of Optical Fiber Networks," *Journal of Lightwave Technology*, vol. 28, no. 4, pp. 662–701, 2010.

[21] L. Galdino, A. Edwards, W. Yi, E. Sillekens, Y. Wakayama, T. Gerard, W. S. Pelouch, S. Barnes, T. Tsuritani, R. I. Killey, D. Lavery, and P. Bayvel, "Optical fibre capacity optimisation via continuous bandwidth amplification and geometric shaping," *IEEE Photonics Technology Letters*, vol. 32, no. 17, pp. 1021–1024, 2020.

[22] R. Ryf, S. Randel, A. H. Gnauck, C. Bolle, A. Sierra, S. Mumtaz, M. Esmaeelpour, E. C. Burrows, R.-J. Essiambre, P. J. Winzer, D. W. Peckham, A. H. McCurdy, and R. Lingle, "Mode-division multiplexing over 96 km of few-mode fiber using coherent 6×6 mimo processing," *Journal of Lightwave Technology*, vol. 30, no. 4, pp. 521–531, 2012.

[23] K. Saitoh and S. Matsuo, "Multicore fiber technology," *Journal of Lightwave Technology*, vol. 34, pp. 55–66, 1 2016.

[24] B. Behera, S. K. Varshney, and M. N. Mohanty, "Design of seven-lp-mode compound-index few-mode-fiber for mode-division-multiplexing transmission," in *2020 International Conference on Communication and Signal Processing (ICCSP)*, pp. 533–537, 2020.

[25] Y. Zhang, F. Ren, X. Fan, J. Zhang, J. Niu, and J. Wang, "Design of weakly-coupled 16-vector-mode coaxial bragg fmf for short-haul communication," *IEEE Access*, vol. 8, pp. 215214–215223, 2020.

[26] A. V. Bourdine, V. A. Burdin, A. E. Zhukov, G. Singh, and V. Janyani, "Simulation-based prediction of 100-μm-core multimode optical fiber bandwidth for 10gbase-lx systems," in *2019 Systems of Signals Generating and Processing in the Field of on Board Communications*, pp. 1–5, 2019.

[27] K. Imamura, K. Mukasa, and R. Sugizaki, "Trench assisted multi-core fiber with large aeff over 100 μm2 and low attenuation loss," in *37th European Conference and Exposition on Optical Communications*, p. Mo.1.LeCervin.1, Optical Society of America, 2011.

[28] T. Hayashi, T. Taru, O. Shimakawa, T. Sasaki, and E. Sasaoka, "Ultra-low-crosstalk multi-core fiber feasible to ultra-long-haul transmission," in *Optical Fiber Communication Conference/National Fiber Optic Engineers Conference 2011*, p. PDPC2, Optical Society of America, 2011.

[29] K. Takenaga, Y. Arakawa, S. Tanigawa, N. Guan, S. Matsuo, K. Saitoh, and M. Koshiba, "Reduction of crosstalk by trench-assisted multi-core fiber," in *Optical Fiber Communication Conference/National Fiber Optic Engineers Conference 2011*, p. OWJ4, Optical Society of America, 2011.

[30] A. Ziolowicz, M. Szymanski, L. Szostkiewicz, T. Tenderenda, M. Napierala, M. Murawski, Z. Holdynski, L. Ostrowski, P. Mergo, K. Poturaj, M. Makara, M. Slowikowski, K. Pawlik, T. Stanczyk, K. Stepien, K. Wysokinski, M. Broczkowska, and T. Nasilowski, "Hole-assisted multicore optical fiber for next generation telecom transmission systems," *Applied Physics Letters*, vol. 105, no. 8, p. 081106, 2014.

[31] T. Sakamoto, K. Saitoh, N. Hanzawa, K. Tsujikawa, L. Ma, M. Koshiba, and F. Yamamoto, "Crosstalk suppressed hole-assisted 6-core fiber with cladding diameter of 125 µm," vol. 2013, pp. 7–9, 2013.

[32] K. Saitoh, T. Matsui, T. Sakamoto, M. Koshiba, and S. Tomita, "Multi-core hole-assisted fibers for high core density space division multiplexing," pp. 164–165, 7 2010.

[33] Y. Amma, Y. Sasaki, K. Takenaga, S. Matsuo, J. Tu, K. Saitoh, M. Koshiba, T. Morioka, and Y. Miyamoto, "High-density multicore fiber with heterogeneous core arrangement," in *2015 Optical Fiber Communications Conference and Exhibition (OFC)*, p. Th4C.4, 2015.

[34] T. Hayashi, T. Nagashima, T. Morishima, Y. Saito, and T. Nakanishi, "Multi-core fibers for data center applications," in *45th European Conference on Optical Communication (ECOC 2019)*, pp. 1–4, 2019.

[35] T. Hayashi, T. Taru, O. Shimakawa, T. Sasaki, and E. Sasaoka, "Design and fabrication of ultra-low crosstalk and low-loss multi-core fiber," *Opt. Express*, vol. 19, pp. 16576–16592, Aug 2011.

[36] R. S. Luís, B. J. Puttnam, A. V. T. Cartaxo, W. Klaus, J. M. D. Mendinueta, Y. Awaji, N. Wada, T. Nakanishi, T. Hayashi, and T. Sasaki, "Time and modulation frequency dependence of crosstalk in homogeneous multi-core fibers," *Journal of Lightwave Technology*, vol. 34, no. 2, pp. 441–447, 2016.

[37] G. Rademacher, R. S. Luís, B. J. Puttnam, Y. Awaji, and N. Wada, "Crosstalk dynamics in multi-core fibers," *Opt. Express*, vol. 25, pp. 12020–12028, May 2017.

[38] T. M. F. Alves and A. V. T. Cartaxo, "Characterization of the stochastic time evolution of short-term average intercore crosstalk in multicore fibers with multiple interfering cores," *Opt. Express*, vol. 26, pp. 4605–4620, Feb 2018.

[39] J. L. Rebola, A. V. T. Cartaxo, T. M. F. Alves, and A. S. Marques, "Outage probability due to intercore crosstalk in dual-core fiber links with direct-detection," *IEEE Photonics Technology Letters*, vol. 31, no. 14, pp. 1195–1198, 2019.

[40] P. J. Winzer and G. J. Foschini, "Mimo capacities and outage probabilities in spatially multiplexed optical transport systems," *Opt. Express*, vol. 19, pp. 16680–16696, Aug 2011.

[41] J. K. Perin, M. Sharif, and J. M. Kahn, "Sensitivity improvement in 100 gb/s-per-wavelength links using semiconductor optical amplifiers or avalanche photodiodes," *Journal of Lightwave Technology*, vol. 34, no. 23, pp. 5542–5553, 2016.

[42] M. Seimetz, *High-Order Modulation for Optical Fiber Transmission*, vol. 1. Springer, Berlin, Heidelberg, 1 ed., 2015.

[43] A. Mecozzi, C. Antonelli, and M. Shtaif, "Kramers-kronig receivers," *Adv. Opt. Photon.*, vol. 11, pp. 480–517, Sep 2019.

[44] A. J. Lowery and J. Armstrong, "Orthogonal-frequency-division multiplexing for dispersion compensation of long-haul optical systems," *Opt. Express*, vol. 14, pp. 2079–2084, Mar 2006.

[45] B. J. C. Schmidt, A. J. Lowery, and J. Armstrong, "Experimental demonstrations of electronic dispersion compensation for long-haul transmission using direct-detection optical ofdm," *Journal of Lightwave Technology*, vol. 26, no. 1, pp. 196–203, 2008.

[46] M. Schuster, S. Randel, C. A. Bunge, S. C. J. Lee, F. Breyer, B. Spinnler, and K. Petermann, "Spectrally efficient compatible single-sideband modulation for ofdm transmission with direct detection," *IEEE Photonics Technology Letters*, vol. 20, pp. 670–672, 5 2008.

[47] A. Mecozzi, C. Antonelli, and M. Shtaif, "Kramers–kronig coherent receiver," *Optica*, vol. 3, pp. 1220–1227, 11 2016.

[48] S. T. Le, K. Schuh, M. Chagnon, F. Buchali, R. Dischler, V. Aref, H. Buelow, and K. M. Engenhardt, "1.72-Tb/s Virtual-Carrier-Assisted Direct-Detection Transmission over 200 km," *Journal of Lightwave Technology*, vol. 36, no. 6, pp. 1347–1353, 2018.

[49] R. S. Luís, G. Rademacher, B. J. Puttnam, C. Antonelli, S. Shinada, and H. Furukawa, "Simple method for optimizing the dc bias of kramers-kronig receivers based on ac-coupled photodetectors," *Opt. Express*, vol. 28, pp. 4067–4075, Feb 2020.

[50] A. J. Lowery, T. Wang, and B. Corcoran, "Clipping-enhanced kramers-kronig receivers," in *2019 Optical Fiber Communications Conference and Exhibition (OFC)*, pp. 1–3, 2019.

[51] D. Kong, E. P. da Silva, Y. Sasaki, K. Aikawa, F. Da Ros, M. Galili, T. Morioka, H. Hu, and L. K. Oxenløewe, "909.5 tbit/s dense sdm and wdm transmission based on a single source optical frequency comb and kramers-kronig detection," *IEEE Journal of Selected Topics in Quantum Electronics*, vol. 27, no. 2, pp. 1–8, 2021.

[52] R. S. Luis, G. Rademacher, B. J. Puttnam, S. Shinada, H. Furukawa, R. Maruyama, K. Aikawa, and N. Wada, "A coherent kramers-kronig receiver for 3-mode few-mode fiber transmission," in *2018 European Conference on Optical Communication (ECOC)*, pp. 1–3, Institute of Electrical and Electronics Engineers Inc., 9 2018.

[53] M. Morsy-Osman, M. Chagnon, M. Poulin, S. Lessard, and D. V. Plant, "224-gb/s 10-km transmission of pdm pam-4 at 1.3 μm using a single intensity-modulated laser and a direct-detection mimo dsp-based receiver," *Journal of Lightwave Technology*, vol. 33, no. 7, pp. 1417–1424, 2015.

[54] M. Y. S. Sowailem, T. M. Hoang, M. Chagnon, M. Morsy-Osman, M. Qiu, S. Paquet, C. Paquet, I. Woods, O. Liboiron-Ladouceur, and D. V. Plant, "100g and 200g single carrier transmission over 2880 and 320 km using an inp iq modulator and stokes vector receiver," *Opt. Express*, vol. 24, pp. 30485–30493, Dec 2016.

[55] F. Chang, K. Onohara, and T. Mizuochi, "Forward error correction for 100 g transport networks," *IEEE Communications Magazine*, vol. 48, no. 3, pp. S48–S55, 2010.

[56] G. Bosco, "Spectrally efficient multiplexing: Nyquist-wdm," in *Enabling Technologies for High Spectral-Efficiency Coherent Optical Communication Networks*, ch. 4, pp. 123–156, John Wiley & Sons, Ltd, 2016.

[57] B. Lin, J. Li, Y. Wan, H. Yang, Y. He, and Z. Chen, "Pre-compensation of mach-zehnder modulator nonlinearity for dd-ofdm system," in *2013 18th OptoElectronics and Communications Conference held jointly with 2013 International Conference on Photonics in Switching*, p. MP1_3, Optical Society of America, 2013.

[58] R. O. J. Soeiro, T. M. F. Alves, and A. V. T. Cartaxo, "Dual polarization discrete changes model of inter-core crosstalk in multi-core fibers," *IEEE Photonics Technology Letters*, vol. 29, no. 16, pp. 1395–1398, 2017.

[59] A. V. T. Cartaxo, R. S. Luís, B. J. Puttnam, T. Hayashi, Y. Awaji, and N. Wada, "Dispersion impact on the crosstalk amplitude response of homogeneous multi-core fibers," *IEEE Photonics Technology Letters*, vol. 28, no. 17, pp. 1858–1861, 2016.

[60] P. Poggiolini and Y. Jiang, "Recent advances in the modeling of the impact of nonlinear fiber propagation effects on uncompensated coherent transmission systems," *Journal of Lightwave Technology*, vol. 35, no. 3, pp. 458–480, 2017.

[61] R. A. Shafik, M. S. Rahman, and A. R. Islam, "On the extended relationships among evm, ber and snr as performance metrics," in *2006 International Conference on Electrical and Computer Engineering*, pp. 408–411, 2006.

[62] M. C. Jeruchim, P. Balaban, and K. S. Shanmugan, *Simulation of Communication Systems*. Boston, MA: Springer US, 2 ed., 1992.

[63] N. Cvijetic, S. G. Wilson, and D. Qian, "System outage probability due to pmd in high-speed optical ofdm transmission," *Journal of Lightwave Technology*, vol. 26, no. 14, pp. 2118–2127, 2008.

[64] T. M. F. Alves, A. V. T. Cartaxo, and J. L. Rebola, "Stochastic properties and outage in crosstalk-impaired ook-dd weakly-coupled mcf applications with low and high skew×bit-rate," *IEEE Journal of Selected Topics in Quantum Electronics*, vol. 26, no. 4, pp. 1–8, 2020.

[65] S. J. Savory, "Digital filters for coherent optical receivers," *Opt. Express*, vol. 16, pp. 804–817, Jan 2008.

[66] B. R. P. Pinheiro, J. L. Rebola, and A. V. T. Cartaxo, "Analysis of inter-core crosstalk in weakly-coupled multi-core fiber coherent systems," *Journal of Lightwave Technology*, vol. 39, no. 1, pp. 42–54, 2021.